

Contrasting soil dynamics in a formerly glaciated and non-glaciated Mediterranean mountain plateau (Serra da Estrela, Portugal)

Gerald Raab^{a,b,*}, Wasja Dollenmeier^a, Dmitry Tikhomirov^a, Gonçalo Vieira^c, Piotr Migoń^d, Michael E. Ketterer^e, Marcus Christl^f, Jamey Stutz^g, Markus Egli^a

^a Department of Geography, University of Zurich, Winterthurerstrasse 190, 8057 Zurich, Switzerland

^b Department of Earth and Environmental Sciences, Dalhousie University, PO BOX 15000, 1459 Oxford Street, Halifax, Canada

^c Centre of Geographical Studies, Institute of Geography and Spatial Planning, University of Lisbon, Rua Branca Edmée Marques, 1600-276 Lisbon, Portugal

^d University of Wrocław, Institute of Geography and Regional Development, pl. Uniwersytecki 1, 50-137 Wrocław, Poland

^e Department of Chemistry and Biochemistry, Northern Arizona University, 700 South Osborne, Flagstaff AZ 86011–5698, USA

^f Department of Physics, Laboratory of Ion Beam Physics, ETH Zürich, Otto-Stern-Weg 5, 8093 Zürich, Switzerland

^g Antarctic Research Centre, Victoria University of Wellington, Kelburn Parade, 6012 Wellington, New Zealand

ARTICLE INFO

Keywords:

Alpine soils
Erosion
Weathering
Fallout radionuclides
Cosmogenic nuclides

ABSTRACT

Few data are available on how soil erosion rates compare between surfaces of different ages because short-term processes often overprint the longer-term erosion signal. This study investigated the soil dynamics among two end-member sites, a formerly glaciated ('young', maximum glacial extent at 22–30 ka BP) and a non-glaciated ('old') area at the Serra da Estrela (Portugal). To disentangle soil distribution rates over different timeframes, isotopes for long-term (¹⁰Be), mid-term (^δ¹³C) and short-term (²³⁹⁺²⁴⁰Pu) periods were applied together with principles of the percolation theory.

The formerly glaciated area has soils with a lower degree of weathering and lower carbon content compared to soils of the 'old', non-glaciated area. The selected isotopes and their distribution along the soil profiles revealed temporal differences in soil mixing process. It is hypothesised that the slightly higher elevation and formerly glaciated sites experienced cryoturbation effects over a longer period, while being less active or absent for the last few decades at the older, non-glaciated soils.

The average long-term (millennia) soil erosion rates correspond to the expected higher rates at the younger surface and lower rates at the older surface. Once the formerly glaciated area became ice-free, soil erosion rates were high and decreased giving rise to average long-term rates of 101–140 [t km⁻² yr⁻¹] for the older surfaces and 176–248 [t km⁻² yr⁻¹] for the younger surfaces. In addition, seasonal freeze–thaw of the soils has persisted over a long period and affected the younger soils more intensively than the older soils. The current (last decades) soil redistribution rates, however, are up to one order of magnitude higher than the millennia rates and are controlled by surface angle and vegetation cover and less by soil texture. The more undulated, non-glaciated older surface had the highest short-term (decades) soil erosion rates in the range of 900–1700 [t km⁻² yr⁻¹], exhibits degrading conditions and relatively shallow soils. The younger soils, however, showed short-term (last few decades) average soil deposition rates of ~ 230 [t km⁻² yr⁻¹]. Human impact (bush fires, grazing) is the cause for the currently strong soil degradation at the non-glaciated area.

1. Introduction

Soil formation is the result of soil production ('gross soil formation') minus all losses due to denudation. Soil production describes the transformation of the parent material (bedrock, morainal deposits, aeolian deposits etc.) into a soil due to chemical and physical

weathering. Soil formation (F_{Soil} , 'net soil formation'; for details, see Egli et al., 2014) can be expressed by.

$$F_{Soil} = P_{Soil} - D_{Soil} \quad (1)$$

where P_{Soil} = soil production and D_{Soil} = soil denudation. Progressive phases occur when soil production is greater than soil denudation and

* Corresponding author at: Department of Geography, University of Zurich, Winterthurerstrasse 190, 8057 Zurich, Switzerland.

E-mail address: gerald.raab@geo.uzh.ch (G. Raab).

regressive phases occur when soil denudation rates are greater than soil production. Denudation (D) consists of chemical (leaching) weathering fluxes (W_{Soil}) and physical erosion fluxes (E_{Soil}) with.

$$D_{\text{Soil}} = W_{\text{Soil}} + E_{\text{Soil}} \quad (2)$$

Chemical and physical weathering and mineral transformation

contribute to progressive soil formation, whereas strong erosion leads to regressive development and thereby to surface lowering and denudation (Raab et al., 2018, 2021). Dixon and von Blanckenburg (2012) demonstrate that global average soil erosion (catchment-wide to profile related data) account for about 50–90 % of D_{Soil} . Thus, E_{Soil} is mostly the primary driver for D_{Soil} .

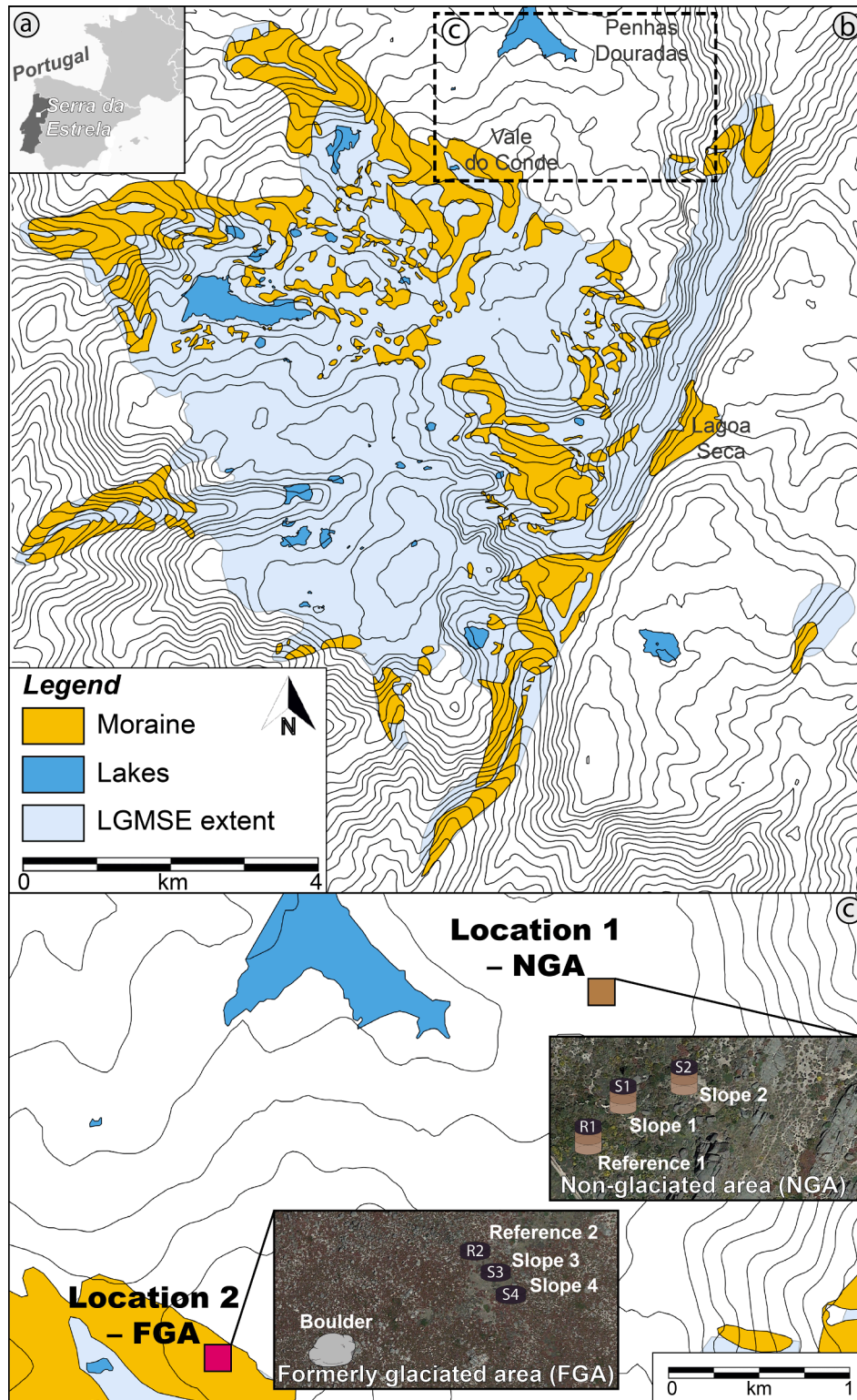


Fig. 1. (a) Location of the Serra da Estrela upland in Portugal, Europe. (b) Map of the Serra da Estrela after Vieira (2004) illustrating the last glacial maximum of the Serra da Estrela (LGMSE, ca. 33.1 ± 5.0 to 30 ± 4.5 ka BP; Vieira, 2008) and current moraine deposits. (c) Close up of the study area and satellite images (Google Earth, 2021) of the sampling sites.

It is generally acknowledged (Heimsath et al., 2009) that soils evolve over time and, under stable topographic conditions, increase their thickness. Relatively young soils (usually < c. 20 kyr) develop fast and exhibit higher soil production (2–3 orders of magnitude; Alewell et al. (2015)), erosion and formation rates than old soils that have already undergone their major developmental phases. At the beginning of alpine soil formation (<c. 3 kyr BP), soil production rates are highest (Egli et al., 2001; Raab et al., 2018, 2019) because the parent material is still fresh, and most minerals are not in equilibrium with atmospheric conditions. Therefore, young soils can usually compensate for soil erosion more easily than mature soils. This compensation capacity can decrease rapidly after 3–4 kyr of soil formation (Egli et al., 2001). Since soil properties change over time, soil erosion rates are expected to change in parallel (Musso et al., 2020). Soil production rates usually increase with increasing catchment-averaged erosion rates, a feedback that enhances soil cover persistence. A high erosion rate is therefore also coupled to young surfaces; due to glacier retreat and fresh exposure of surfaces or to a constant rejuvenation of the surface due to erosion and, thus, the appearance of less or unweathered rock material. At the plot or hillslope scale, previous studies reveal large variations in the relative importance of physical and chemical processes that break apart or dissolve in-situ bedrock (e.g., Dixon and Amundson, 2009; Heimsath et al., 2012, 2020).

To identify soil property differences and, thus, temporal variations of erosion during soil evolution, a comparable landscape setting is required. Upland plateaus may provide suitable conditions for a comparison of soils having different formation times, but in comparable environmental conditions. Plateau icefields with their specific hypsometry makes them highly sensitive to climate change (Rea and Evans, 2005). When the equilibrium line altitude (ELA) lies above the plateau edge, then glaciers will melt relatively rapidly, and when the ELA decreases the glaciers will expand substantially. Consequently, landscapes with former plateau glaciers may exhibit distinct geomorphic evidence of ELA changes and show spatio-temporal signals of climate variability. In such areas, relatively young surfaces, where landscape has been primarily controlled by former glacial processes, can be close to areas that are much older and potentially non-glaciated. How surface erosion varies between these different types of sites is largely unknown so far. However, in the Mediterranean region, long-term changes in sediment dynamics and, thus, soil erosion show similarities to Holocene climatic oscillation (Bellin et al., 2013). Yet, the Mediterranean region is commonly reported as the European region that is most affected by land degradation (e.g., deforestation, overgrazing, quarrying, monoculture) over millennia (Cammeraat and Imeson, 1998; Wainwright and Thornes, 2004). Therefore, land degradation processes of the past few decades (or centuries) may distinctly overprint the multi-millennia erosion signal. Consequently, soil erosional processes are difficult to temporally disentangle.

The aim of this investigation is to determine short- and long-term soil redistribution signals to quantify the corresponding soil redistribution rates and to relate them to differences in soil characteristics between two end-member sites in the Mediterranean: A formerly glaciated area (FGA) and a non-glaciated area (NGA; Fig. 1b) during the local last glacial maximum of the Serra da Estrela (LGMSE 30–33 ka BP; LGM; 27.5–23.3 ka BP after Hughes and Gibbard (2015); 26.5 to 19 ka BP after Clark (2009); some local LGMs occurred earlier, 30–32 ka BP, Oliva et al., (2019)) (Vieira, 2008; Vieira et al., 2021). The glaciers disappearance inflicted a shift in denudation forces on the formerly ice-covered bedrock (Reiter et al., 2013; Williams and Koppes, 2019). During the LGM the bedrock was shaped by abrasive erosion (abrasion, quarrying). However, the rock-degradation process became more weathering-dominated once the surface was exposed to chemical near-surface processes. Since then, bedrock minerals have been transformed by in situ weathering through chemical, physical, and biological processes.

At the Serra da Estrela study area, we have two contrasting hypotheses: i) surfaces beyond the limits of glaciation should be closer to an equilibrium with the environmental conditions with respect to soil

erosion and soil production, while at the FGA, landscape is not yet in equilibrium. Thus, higher erosion rates and higher geomorphic dynamics should be expected in the FGA. We also assumed that short- (over decades) and long-term (millennial) erosion rates independently reflect these assumed soil dynamic differences. ii) An alternative and contrasting hypothesis is that, given the landscape setting with FGA at the highest and innermost part of the mountain plateau, the FGA has suffered less vegetation degradation due to human impact than the NGA which gave rise to a lower erosion rate.

2. Study area and sampling strategy

2.1. Study area

We investigated soil characteristics of a formerly glaciated and non-glaciated area of the UNESCO Geopark at the Serra da Estrela, Portugal (Fig. 1a). Today, the upland morphology of the Serra da Estrela is dominated by glacial landforms in the western and highest plateau, by granitic landforms from selective weathering (e.g., tors) in the eastern plateau and margins of the western plateau (Lautensach, 1929; Daveau 1971; Vieira, 2004, Vieira et al., 2017). Our two study sites are in the western plateau of the Serra da Estrela that was mostly glaciated during the LGM (Vieira et al., 2021, Fig. 1b,c). The Serra da Estrela is in the central north of Portugal and is a part of the Iberian Central Cordillera. The granite massif is elongated in a NE-SW direction, creating a condensation barrier to the moist air masses from the Atlantic (Mora and Vieira, 2020). Summers are arid and winters are humid. The annual precipitation is about 1510 mm (IPMA, 2021; Penhas Douradas, 1300 m a.s.l.) with an annual average temperature of 4 °C at the summit (Vieira, 2008; Mora, 2010). Two steep fault-generated escarpments constitute the boundaries of the mountain massif with a relative elevation of over 1000 m (Migoñ and Vieira, 2014).

The highest part of Serra da Estrela is divided into two plateaus by the Zêzere and Alforfa valleys, both carved along a NNE-SSW tectonic lineament. The eastern plateau lies just below 1750 m a.s.l., while the western plateau has the highest elevation of Portugal's mainland with an altitude of 1993 m a.s.l. Lautensach (1929), Daveau (1971) and Vieira et al. (2004) showed that during the LGM the western plateau area was covered by a plateau icefield having several radiating valley glaciers (Fig. 1b). In contrast, on the eastern plateau only a small lee-side glacier occurred. Periglacial conditions prevailed in the upper plateaus outside the glaciated areas during the Pleistocene cold periods, with medium and fine-grained granite variants showing blockslopes and blockfields and abundant slope deposits (stratified, head-type) in the valleys (Vieira and Nieuwendam, 2020). Micromorphological analysis of slope deposits showed that seasonal frost played a significant role in slope dynamics, especially above 650 m a.s.l., with permafrost occurring above 1300 m a.s.l. (Nieuwendam et al. 2020). In general, soils on the western, granite-dominated plateau can be described as Lithosols (Leptosols after WRB), while on the schist bedrock at lower altitude Cambisols are found (Connor et al., 2012; Table 1).

Most knowledge on the landscape history of the Serra da Estrela after the deglaciation comes from the work conducted at the Charco da Candieira sediment cores at 1400 m a.s.l. (Van den Brink and Janssen, 1985; Van der Knaap and Van Leeuwen, 1995, 1997; Connor et al., 2012). Analysis of sediment cores identified the following phases of environmental changes (Van der Knaap and Van Leeuwen, 1995, 1997):

- i. the period from 14,800 to 11600 cal BP showed an alternation between steppe vegetation and open forests,
- ii. the period from 11,600 to 9500 cal BP was characterised by the development of xerothermic oak-dominated forests under a warmer and drier climate compared to the previous one,
- iii. the period from 9500 to 6400 cal BP experienced again a cooler and moister climate than the previous period with the forests shifting to mesothermic conditions and with the first signs of human influence,
- iv. during the period from 6400 to 3400 cal BP the forest dynamics are affected by grazing and deforestation,
- v. the period

Table 1
Study sites characteristics.

Site	Coordinates (WGS 84)		Elevation [m a.s.l.]	Geologic substrates	Vegetation	Aspect [°]	Overall surface slope [°]	Slope at the soil pit [°]	Soil type (WRB)
Location 1 (non-glaciated)									
Reference (R1)	N	W	1495	Granite/ granodiorite	shrubs, grassland	–	2°	0°	Cambisol
Slope 1 (S1)	N	W	1492	Granite/ granodiorite	grassland	Northwest	2–5°	10°	Regosol
Slope 2 (S2)	N	W	1494	Granite/ granodiorite	patches of grassland	Northwest	2–5°	20°	Cambisol
Location 2 (glaciated)									
Reference (R2)	N	W	1651	Granite/ granodiorite	grassland	–	3°	0°	Cambisol
Slope 3 (S3)	N	W	1655	Granite/ granodiorite	grassland	East	3–7°	5°	Cambisol
Slope 4 (S4)	N	W	1645	Granite/ granodiorite	grassland	East	3–7°	5°	Cambisol

from 3400 to 970 cal BP shows large scale deforestation, followed by partial forest recovery, and *vi.* the period from 970 to 40 cal BP shows a strong decrease of the natural vegetation, accompanied by soil erosion, grazing, burning, agriculture and silviculture.

Connor et al. (2012) analysed the same sediment core for the reconstruction of the fire history of the landscape. They found that fires are frequent in the Serra da Estrela since the Late Pleistocene and that they are part of the ecological dynamics of the region. Several periods of increased fire activity were identified, followed by stability phases which led to the recovery of the vegetation. Despite the regular presence of fire, the charcoal records show two major shifts in the fire regime with a distinct increase in fire activity: one at the beginning of the Holocene (~12000 to 11000 cal BP) and another in the mid-late Holocene (~3500 to 2500 cal BP). Present day bush fires are a major environmental phenomenon in the Serra da Estrela, as in the entire mainland of Portugal.

2.2. Sampling locations and strategy

To assess the soil development history in the Serra da Estrela plateau, the sampling locations were selected in the northern area of the western plateau between the Penhas Douradas (~1492 – 1495 m a.s.l.) and Vale do Conde (~1645 – 1655 m a.s.l.). The Penhas Douradas represents the ice-free margin with a distinct tor and bornhardt landscape (thus, large residual rock pillars that are still rooted in the bedrock (Linton, 1955)). The Vale do Conde site is in a marginal moraine with widespread grass covering the surface of shallow soils and marks the boundary between the past plateau ice-field and the non-glaciated bornhardt landscape.

Six representative soil sites for the western plateau (3 in the FGA and 3 in the NGA) were selected. At each soil site, 4 samples per soil depth were taken. For the determination of short-term erosion rates (last six

decades) using $^{239+240}\text{Pu}$, reference sites were selected, on a flat surface ('R') and sites on a slope surface ('S'), respectively. To assess the mid-term soil stability (centuries), $\delta^{13}\text{C}$ was measured in all soil samples. For the investigation of long-term soil stability (millennia) or mixing processes (e.g., cryoturbation) using meteoric ^{10}Be , the reference site ('R2') at the FGA was selected. The soils (all unploughed) at our study sites are mostly weakly developed (Fig. 2). The seasonally dry and shallow (~30 cm depth) soils are rather poorly structured. They can be classified mostly as Cambisols (R1, S2, R2, S3, S4) and Regosols (S1) according to the World Reference Base for Soil Resources (WRB) (Table 1; Fig. 2; IUSS Working Group WRB, 2015).

One moraine boulder was sampled in the proximity to the soil pits of the FGA (Fig. 1c) to gain a better local understanding of the glacial retreat time and a reasonable timeframe for the earliest onset of soil formation. About 2 kg samples of rock were taken from the uppermost rock surface (1 – 3 cm thick) using an electric stone saw or chisel and hammer. The topographic shielding, dip and dip-direction of the rock surface were recorded. All sampling sites were recorded by global positioning system (GPS) and verified with topographic maps.

3. Materials and methods

3.1. General physical and chemical analyses

All bulk samples were oven dried (70 °C) for 36 h and sieved to < 2 mm (fine earth) to determine the proportion of rock fragments (soil skeleton). Soil bulk density was obtained from the dry weight of the 100 cm³ soil cores before fine milling (<50 μm). Grain size analysis of the coarser particles (2000–32 μm) was performed by wet sieving. Finer particles (<32 μm) were analysed using a X-ray sedimentometer (Sedi-Graph 5100).

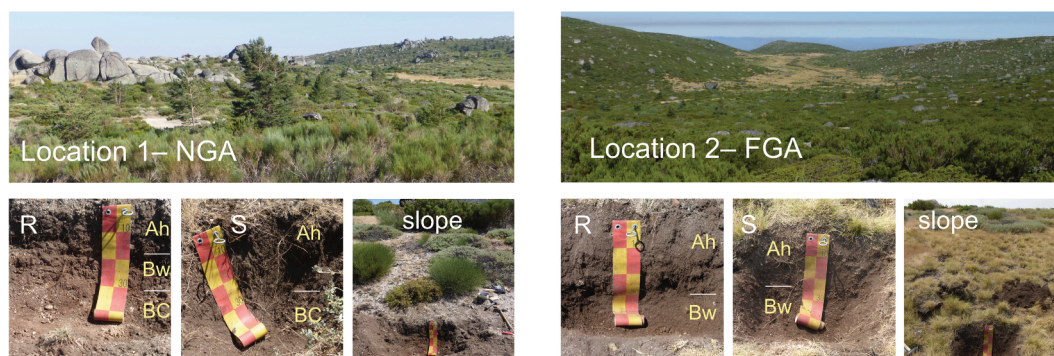


Fig. 2. Landscape settings of location 1 and 2 together with photos of a reference (R), a slope soil profile (S) and the slope vegetation cover. The soil profiles are given with the corresponding soil horizons.

Soil pH (in 0.01 M CaCl₂) was measured twice on air-dried fine-earth samples and a soil:solution ratio of 1:2.5. Concentrations of Al, Fe, Mn and Si were determined (in duplicate) after a treatment of the soil with NH₄-oxalate (buffered at pH 3) (McKeague et al., 1971). Element concentrations were measured using atomic absorption spectroscopy (AAS) (contrAA 700 BU, Analytikjena). The oxalate (Al_o, Fe_o, Mn_o, Si_o) extracts both the poorly crystalline phases and some of the organic phases, but normally does not dissolve the strong humus-metal complexes (Mizota and van Reeuwijk, 1989). The citrate-bicarbonate-dithionite (CBD; after Mehra and Jackson, 1958) soluble forms of Al, Fe and Si were also measured using AAS.

Loss on ignition (LOI) was determined by dry-ashing the milled fine-earth for Pu-analysis (16 h, 550 °C). The measurement of major and trace element contents in the soil was performed by X-ray fluorescence (XRF) (Beckhoff et al., 2006). About 5 g of milled fine earth was analysed as loose powder in sample cups using an energy dispersive XRF spectrometer (SPECTRO X-LAB 2000, SPECTRO Analytical Instruments, Germany). A soil standard (NCS DC 73326) was used for quality control.

The total carbon (C_{tot}) that equals organic C (C_{org}; acidic soils and, thus, no carbonates present) and total nitrogen contents were obtained by measuring about 0.01 g milled soil material in tin capsules using a Thermo Fisher Scientific Flash HT Plus elemental analyser with SmartEA coupled to a ConFlo IV to Delta V Plus isotope ratio mass spectrometer. The δ¹³C isotopic ratios were measured using a Picarro analyser (Combustion Module-Cavity Ring Down Spectroscopy (CM-CRDS), Sunnyvale, California, USA). Soil powder of the milled fine earth was weighed (~0.1 g) into tin capsules and combusted at 950 °C. The released CO₂ was measured with a CRDS analyser (G2131-i).

3.2. Chemical separation and ¹⁰Be analysis

For *in-situ* ¹⁰Be extraction, the rock sample of the boulder was crushed and about 0.4 kg of the 0.6 – 0.25 mm fraction was retained. The material was then processed according to standard practice (Kohl and Nishiizumi, 1992), which is summarized as follows. The retained fraction was treated with *aqua regia* (1:4.22 of 65% HNO₃ to 32% HCl) for up to 36 h to eliminate iron oxides, organic matter and carbonates. The remaining mineral assemblage underwent a 1 h treatment with 0.4% HF. A flotation system after Kitchener (1984) was used to physically separate mica and feldspar from quartz. Remaining contaminants were removed with 4% HF leaching cycles. The resulting 30 g of pure quartz was spiked with a ⁹Be-carrier solution (Scharlau, BE03460100) and together dissolved in 40% HF. We isolated Be using anion (Bio-Rad AG1-X8 resin) and cation (Bio-Rad AG50-X8 resin) exchange columns (von Blanckenburg et al., 1996).

For meteoric ¹⁰Be extraction, 2 g of fine milled soil was spiked with a ⁹Be-carrier solution (Fluka TraceCERT 41856) and leached twice in 16% HCl overnight. The leachates were centrifuged to remove any solid material and combined. Beryllium was separated with cation exchange columns (Bio-Rad AG50-X8 resin) followed selective coprecipitation.

The resulting Be(OH)₂ gel of both procedures (meteoric and *in-situ*) was dehydrated on a hot plate at 70 °C overnight and at 120 °C for ~ 5 h. The Be(OH)₂ was converted to BeO by calcination at 850 °C for two hours. The final BeO was mixed with niobium (Nb) powder prior pressing into copper (Cu)-targets and measured with accelerator mass spectrometry (AMS, Tandy) at the ETH Laboratory of Ion Beam Physics. The ETH used ¹⁰Be standard S2007N and S2010N with a nominal value of ¹⁰Be/⁹Be = 28.1 × 10⁻¹² and ¹⁰Be/⁹Be = 3.3 × 10⁻¹² calibrated to the Nishiizumi standard ICN01-5-1 with a revised nominal value of 2.709 × 10⁻¹¹ (Nishiizumi et al., 2007; Kubik and Christl, 2010; Christl et al., 2013). Both standards have an associated ¹⁰Be half-life of 1.387 ± 0.012 Myr (Chmeleff et al., 2010; Korschinek et al., 2010). The 1σ error of S2007N and S2010N are 2.7% (Christl et al., 2013) and 2.2% respectively. The measured ¹⁰Be/⁹Be ratios were corrected for the ¹⁰Be contribution of the Be-carrier.

3.3. Surface exposure dating using *in-situ* ¹⁰Be

Exposure ages based on *in-situ* ¹⁰Be contents were calculated using the cosmogenic nuclide online calculator v3.0 (Balco et al., 2008). The program uses a ¹⁰Be half-life of 1.387 ± 0.0012 Ma (Chmeleff et al., 2010; Korschinek et al., 2010). The production rate was corrected for latitude and altitude after the scaling scheme of Stone (2000) and further corrected for the sample thickness according to the depth profile of Brown et al. (1992) with an effective radiation attenuation length of 160 g cm⁻² of Gosse and Philips (2001) and a constant rock density of 2.65 g cm⁻³. Related effects of geomagnetic field variations on the *in-situ* ¹⁰Be ages can be assumed to be negligible (Masarik et al., 2001; Pigati and Lifton, 2004).

3.4. Determination of short-term soil erosion rates using ²³⁹⁺²⁴⁰Pu

We used ²³⁹⁺²⁴⁰Pu to assess soil redistribution (erosion or deposition) rates of the recent past (last ~ 60 years; mainly emitted during nuclear weapons tests with a maximum in 1963–1964; Wallbrink and Murray, 1993). Average soil redistribution rates are calculated based on the differences in Pu-activity [Bq m⁻²] among inclined investigation sites (e.g., slopes) and a flat reference site. The inventory (*I*) of the ²³⁹⁺²⁴⁰Pu activities [Bq m⁻²] serves as a basis for the calculation of soil redistribution rates (erosion/accumulation):

$$I = \frac{1}{a} \sum_i M_i C_i \quad (3)$$

where *a* = horizontal cross-sectional area [m²], *M_i* = mass [kg] of the *i*-th sample depth increment and *C_i* = activity [Bq kg⁻¹] of the *i*-th sub-sample depth increment. Redistribution rates of soils were then obtained by comparing the isotope inventory for an investigation point with a stable local reference inventory where neither soil erosion nor soil accumulation is expected. We used two of the most common models to convert ²³⁹⁺²⁴⁰Pu inventories into soil redistribution rates. The profile distribution model (PDM) for uncultivated soils after Walling and He (1999) and Zhang et al. (1990) uses a simple numerical (exponential) function to represent the vertical distribution of the measured Pu. The inventory method (IM) according to Lal et al. (2013) calculates the loss of soil also for uncultivated and unploughed soils.

3.5. Soil sample preparation and ²³⁹⁺²⁴⁰Pu activity analysis

The extraction of fallout plutonium from soil was done according to Ketterer et al. (2004). Briefly, 5–7 g of sample was dry-ashed (16 h, 550 °C) and spiked with 0.005 Bq of a ²⁴²Pu solution (Harwell laboratory; 0.00253 [Bq] or 17.07 [pg]). The sample was leached with 16 [mol l⁻¹] nitric acid overnight at 80 °C. The leachate was filtered from solids and plutonium was recovered on TEVA resin (EiChrom, Ketterer et al., 2011).

The isotopes masses 235, 238, 239, 240 and 242 were analysed at the Northern Arizona University using a Thermo X2 quadrupole ICP-MS instrument equipped with a ESI Scientific Apex HF sample introduction system with FEP Teflon concentric nebulizer. A detection limit of 0.002 [Bq kg⁻¹] of ²³⁹⁺²⁴⁰Pu was obtained for samples of 7 g of dry-ashed material, while ²³⁹⁺²⁴⁰Pu activities >1 [Bq kg⁻¹] provided measurement error <3 %. The individual mass ratios were corrected to the mass bias and ²³⁸U^{H+} isobar. Data quality was evaluated through the analysis of blanks (soils or rocks devoid of Pu), sample duplicates and soil standards with known ²³⁹⁺²⁴⁰Pu activity.

3.6. Chemical weathering indices and semi-quantitative relative dating

Several weathering indices were used to characterise mineral alteration and the weathering degree of the soils (Table S1). We tested these geochemical weathering proxies as potential tracers of erosion; among

them were the often-used Chemical Index of Alteration (CIA; Nesbitt and Young, 1982), Chemical Index of Weathering (CIW; Harnois, 1988), the Weathering Index of Parker (WIP; Parker, 1970), B-index (Kronberg and Nesbitt, 1981) and the silica-aluminium ratio (SA; Ruxton, 1968).

3.7. Soil formation prediction using the percolation theory

Recent research shows that chemical weathering and, thus, soil formation are in most cases limited by water availability and solute transport (Hunt et al., 2015; Yu and Hunt, 2017; Yu et al., 2019). Soil depth reflects soil formation and therefore integrates soil production and erosion. According to the percolation theory, the soil production function can be described as follows:

$$\frac{dx}{dt} = R - E(t) = \frac{1}{1.87} \frac{x_0}{t_0} \left(\frac{t}{t_0}\right)^{-0.87} - E(t) = \frac{1}{1.87} \frac{I(t)}{\phi} \left(\frac{x}{x_0}\right)^{-0.87} - E(t) \quad (4)$$

Table 2

Physical soil characteristics of reference sites (further data in Table S2).

Sample #	Soil Depth [cm]	Soil skeleton (>2 mm) [wt%]	Sand [%]	Silt [%]	Clay [%]	Bulk density [g cm ⁻³]	Munsell colour (dry)
Location 1 (NGA)							
R1-P1-P1							
SdE-1	0–5	56.6	n.d.	n.d.	n.d.	0.58	10 YR 3/2
SdE-2	5–10	75.6	n.d.	n.d.	n.d.	0.73	10 YR 4/3
SdE-3	10–15	51.2	40.8	28.8	29.2	0.71	10 YR 4/2
SdE-4	15–20	53.9	n.d.	n.d.	n.d.	0.65	10 YR 4/2
SdE-5	20–25	57.5	n.d.	n.d.	n.d.	0.60	10 YR 4/2
R1-P1-P2							
SdE-6	0–5	43.1	n.d.	n.d.	n.d.	0.59	10 YR 4/2
SdE-7	5–10	60.8	n.d.	n.d.	n.d.	0.75	10 YR 4/2
SdE-8	10–15	53.6	29.2	36.4	33.2	0.79	10 YR 3/2
SdE-9	15–20	57.3	n.d.	n.d.	n.d.	0.80	10 YR 4/2
SdE-10	20–25	54.5	n.d.	n.d.	n.d.	0.90	10 YR 4/2
R1-P2-P1							
SdE-11	0–5	57.0	n.d.	n.d.	n.d.	0.59	10 YR 4/2
SdE-12	5–10	32.0	32.0	31.2	36.8	0.59	10 YR 3/2
SdE-13	10–15	47.6	29.2	32.8	36.4	0.68	10 YR 3/2
SdE-14	15–20	49.2	n.d.	n.d.	n.d.	0.66	10 YR 3/2
SdE-15	20–25	37.9	33.2	27.6	39.2	0.60	10 YR 3/2
R1-P2-P2							
SdE-16	0–5	47.3	n.d.	n.d.	n.d.	0.56	10 YR 4/2
SdE-17	5–10	52.0	n.d.	n.d.	n.d.	0.74	10 YR 3/2
SdE-18	10–15	48.9	24.8	36.0	39.2	0.85	10 YR 3/2
SdE-19	15–20	50.2	38.8	26.0	35.2	0.74	10 YR 3/2
SdE-20	20–25	51.3	38.4	34.8	25.6	0.82	10 YR 3/2
Location 2 (FGA)							
R2-P1-P1							
SdE-61	0–5	17.3	42.0	22.8	34.8	0.53	10 YR 3/2
SdE-62	5–10	29.6	19.2	39.6	40.8	0.64	10 YR 3/2
SdE-63	10–15	23.2	28.4	27.6	44.0	0.70	10 YR 3/2
SdE-64	15–20	31.2	22.0	37.2	40.4	0.74	10 YR 3/2
SdE-65	20–25	32.7	36.0	19.2	44.8	0.77	10 YR 3/2
SdE-66	30–35	69.1	n.d.	n.d.	n.d.	0.97	10 YR 4/2
R2-P1-P2							
SdE-67	0–5	20.2	32.4	30.0	37.6	0.68	10 YR 3/2
SdE-68	5–10	25.7	18.0	36.4	44.4	0.62	10 YR 3/2
SdE-69	10–15	28.3	32.0	22.0	46.0	0.67	10 YR 3/2
SdE-70	15–20	44.9	24.0	34.4	41.2	0.81	10 YR 3/2
SdE-71	20–25	46.3	19.6	30.4	47.2	0.75	10 YR 3/2
SdE-72	30–35	68.9	n.d.	n.d.	n.d.	1.07	10 YR 3/2
R2-P2-P1							
SdE-73	0–5	26.6	33.6	20.8	45.6	0.69	10 YR 4/2
SdE-74	5–10	35.5	30.0	30.8	38.4	0.77	10 YR 4/2
SdE-75	10–15	28.8	18.0	42.8	37.2	0.65	10 YR 3/2
SdE-76	15–20	34.9	29.2	25.2	45.6	0.71	10 YR 3/2
SdE-77	20–25	63.4	26.0	34.0	38.0	1.01	10 YR 3/2
R2-P2-P2							
SdE-78	0–5	31.9	20.0	29.2	49.6	0.60	10 YR 4/2
SdE-79	5–10	34.8	34.4	33.6	31.6	0.71	10 YR 3/2
SdE-80	10–15	31.1	13.2	46.8	37.2	0.72	10 YR 3/2
SdE-81	15–20	26.3	34.0	31.6	33.2	0.67	10 YR 3/2
SdE-82	20–25	34.1	20.4	43.5	35.2	0.71	10 YR 3/2

with $I(t)/\phi$ as the net infiltration, E as (soil) erosion, R as soil production. The variable x represents soil depth. The spatial scale x_0 relates to a grain diameter (median grain diameter of a soil material), x_0/t_0 is the water flow rate. By knowing the age t of the soil and its thickness, the average (soil) erosion rates over the entire soil development phase can be determined.

4. Results

4.1. General physical and chemical soil characteristics

The soil thickness at the NGA reference sites was about 40 cm (down to the C horizon), and at the FGA reference site about 40–50 cm (until a R horizon appeared). The vegetation at both sites was dominated by grass and shrubs (Table 1). Profile differentiation in all soil pits was relatively weak. The average soil skeleton content at the NGA was

mostly over 50 [wt. %], and ~ 35 [wt. %] at the FGA. The average grain size distribution at the FGA sites was about 27% sand, 32% silt and 41% clay, at the NGA the respective distribution was one third each (Table 2).

The soil bulk density was on average $0.7 \text{ [g cm}^{-3}\text{]}$, similar at both areas and increased with soil depth (Fig. 3a,b). The soil colour (dry) was similar at all sites (Table 2; Table S2). The soils were strongly acidic in both areas (lowest pH is 3.35 at NGA, 3.74 at FGA); pH increased with depth (Fig. 3a,b; Table 3). The maximum total carbon content at the NGA was up to four times higher (e.g., sample SdE-31, Table S3) compared to the FGA. The highest average total carbon content ($\sim 16\%$) was found in the topsoil of slope 1 (S1). Total nitrogen ranged from $\sim 0.4\%$ to 0.9% at the NGA while it varied between $\sim 0.5\%$ and $\sim 0.6\%$ at FGA. The depth trends of slope 2 (S2) slightly differed in soil physical and chemical properties compared to S1 and R1. The soil at S2 had a higher bulk density, higher pH, and the lowest C and N content of all measured samples. Only the $\delta^{13}\text{C}$ values at S2 (Table 3; Table S3; Fig. 3a) were within a comparable range to the other investigated soils. However, the total carbon content in S2 ($C_{\text{tot}} 0.77\text{--}5.55\%$) contrasted the other two sites at the NGA and matched the ranges measured at the FGA.

The poorly-crystalline phases content differed among the two end-member sites (Fig. 4). The content of all extracted elements (Al_0 , Fe_0 , Si_0 , Mn_0) was highest at the reference site of the NGA (Fig. 4, Table 3). The dithionite extractable Al and Si contents were also highest at the NGA reference site (Fig. 4). Throughout the profile, the Fe_d content was higher at the FGA and increased with depth before starting to decrease at about 17.5 cm soil depth (Fig. 4). At both areas, the Al_d content increased whereas the Si_d content decreased with depth (Fig. 4). The crystalline oxyhydroxide content of Fe (Fe_{cry} ; calculated as the difference between the dithionite- and oxalate-extractable forms) remained constant in a range of $\sim 0.5 \text{ [g kg}^{-1}\text{]}$ (NGA) and $\sim 1.9 \text{ [g kg}^{-1}\text{]}$ (FGA) with depth. Only at the FGA reference site Fe_{cry} increased at about 22.5 cm to $\sim 4 \text{ [g kg}^{-1}\text{]}$.

4.2. Total element contents and weathering indices

A relatively high variability of major and trace elemental depth-

trends was found in the NGA, while the soil profiles in the FGA often exhibited a trend (Table 4; Table S4). For example, the SiO_2 content of R2 decreased from 55% in the uppermost layer to 48% in the lowermost layer at FGA. At the NGA, the content remained in a relatively narrow range. At the FGA the Al_2O_3 increased with depth from $\sim 20\%$ to $\sim 30\%$ (e.g., S4). Again, S2 had a different chemical trend compared to R1 and S1. The soils were characterised by high Al_2O_3 content that ranged from ~ 34 to 40% at site S2. Interestingly, relatively immobile elements (e.g., Ti, Zr, Cr) were homogeneously distributed throughout the soil profile at site R2 at the FGA. For example, TiO_2 remained within its average of $0.51 \pm 0.02\%$ at R2. The highest TiO_2 content (0.67%) was found in the NGA (R1).

These elemental patterns were also reflected in the calculated weathering patterns (Table S1, Fig. 5). The B-index, CIA and SA all indicated a higher degree of weathering in the NGA, with S2 having the highest weathering degree. In the FGA, S4 was less weathered compared to R2 and S3 which had similar trends.

4.3. Qualitative soil stability ($\delta^{13}\text{C}$)

The $\delta^{13}\text{C}$ signature of all samples ranged in general from -28.87% to -26.75% and increased with depth (Fig. 3a). The $\delta^{13}\text{C}$ -signature was within the range of C3-grasses (-20% to -30%) and was typical for perennial cool and dry areas. The anticipated negative correlation (see section 3.1) between $\delta^{13}\text{C}$ and C_{org} was only encountered at the non-glaciated sites of R1 ($R^2 = 0.39$; p -value = 0.003) (Fig. 6). The $\delta^{13}\text{C}$ and C_{org} data of S2 indicated a positive correlation ($R^2 = 0.33$; p -value = 0.008). In the FGA the $\delta^{13}\text{C}$ and C_{org} data showed a large variability and did not exhibit a clear correlation ($R^2 < 0.09$), although both $\delta^{13}\text{C}$ and C_{org} were in the same range as at S2.

4.4. Short-term ($^{239+240}\text{Pu}$) and average long-term soil redistribution rates

The average $^{240}\text{Pu}/^{239}\text{Pu}$ atomic ratios at all depths were within the characteristic signature of the fallout of the northern hemisphere (0.180

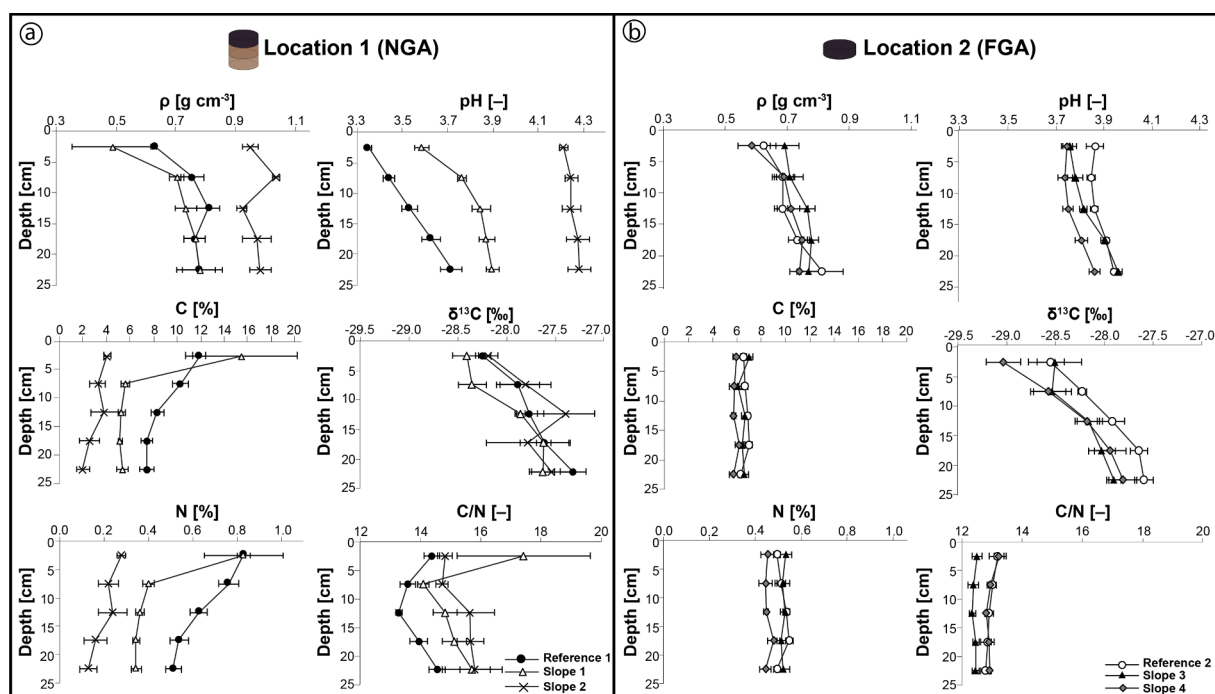


Fig. 3. Selected physical and chemical properties in the profiles of the non-glaciated (a) and formerly glaciated area (b). Values represent the average ($n = 4$) for the according depth increment at each location. The values for the depth range 30–35 cm at the FGA site (see Table 2 and 3) were excluded for better visual comparability.

Table 3
Chemical characteristics of reference soil sites (further data in Table S3).

SSample #	Depth [cm]	pH (CaCl ₂) [-]	C* [%]	δ ¹³ C* [‰]	C** [g kg ⁻¹]	N** [g kg ⁻¹]	C/N [-]	Al _o [g kg ⁻¹]	Fe _o [g kg ⁻¹]	Mn _o [mg kg ⁻¹]	Si _o [mg kg ⁻¹]	Al _o + ½ Fe _o [g kg ⁻¹]	Al _d [g kg ⁻¹]	Fe _d [g kg ⁻¹]	Si _d [mg kg ⁻¹]	Fe _o /Fe _d [-]
Location 1 (NGA)																
R1-P1-P1																
SdE-1	0–5	3.37	11.0	-28.37	107.6	7.8	13.8	1.54	3.24	27.5	108.7	3.16	2.90	3.91	937	0.83
SdE-2	5–10	3.40	11.5	-28.47	111.0	7.7	14.4	1.78	4.93	36.4	87.1	4.24	3.60	3.98	821	1.24
SdE-3	10–15	3.55	8.9	-28.05	95.7	7.2	13.3	2.50	5.12	15.0	166.6	5.06	4.50	4.07	1059	1.26
SdE-4	15–20	3.62	6.7	-28.28	60.9	4.3	14.3	1.72	5.52	7.9	104.9	4.48	3.39	4.62	602	1.19
SdE-5	20–25	3.66	5.5	-27.60	69.3	5.0	14.0	2.18	4.66	10.2	140.6	4.51	4.45	4.74	509	0.98
R1-P1-P2																
SdE-6	0–5	3.37	9.1	-28.02	117.3	8.4	14.0	1.56	5.06	15.7	88.9	4.09	3.43	3.95	943	1.28
SdE-7	5–10	3.39	12.3	-27.95	115.5	8.7	13.3	1.96	6.18	16.8	83.6	5.04	3.64	4.14	1047	1.49
SdE-8	10–15	3.44	9.5	-27.89	88.9	6.7	13.2	1.78	7.10	16.3	90.1	5.33	3.43	3.08	830	2.30
SdE-9	15–20	3.53	8.1	-27.70	80.2	6.1	13.2	1.71	6.66	12.5	120.7	5.04	4.44	4.55	785	1.46
SdE-10	20–25	3.61	6.2	-27.47	66.8	4.6	14.5	1.70	7.21	4.1	115.1	5.30	4.24	4.80	454	1.50
R1-P2-P1																
SdE-11	0–5	3.34	14.0	-28.23	133.7	8.9	15.0	1.55	3.57	10.8	48.8	3.34	2.39	3.98	795	0.90
SdE-12	5–10	3.47	7.6	-27.44	101.7	7.7	13.3	2.31	5.19	9.8	89.9	4.91	3.47	4.60	695	1.13
SdE-13	10–15	3.54	9.7	-27.77	76.9	5.8	13.3	2.17	4.09	4.6	78.5	4.22	2.88	4.63	347	0.88
SdE-14	15–20	3.63	7.7	-27.30	85.2	6.3	13.6	2.39	5.62	8.5	150.3	5.20	4.82	4.92	251	1.14
SdE-15	20–25	3.82	7.7	-27.06	94.4	6.2	15.3	4.16	8.16	8.3	110.2	8.24	8.89	8.33	435	0.98
R1-P2-P2																
SdE-16	0–5	3.33	10.0	-28.35	118.7	8.1	14.7	1.69	10.00	5.5	75.1	6.69	2.56	4.63	1019	2.16
SdE-17	5–10	3.51	8.9	-27.69	84.7	6.4	13.3	1.88	10.29	4.8	50.0	7.02	3.11	4.62	727	2.23
SdE-18	10–15	3.61	7.8	-27.36	72.8	5.5	13.3	2.31	12.09	5.6	104.2	8.35	3.62	5.04	608	2.40
SdE-19	15–20	3.74	7.7	-27.17	72.7	5.0	14.6	2.60	11.70	9.7	81.8	8.45	4.64	5.35	480	2.19
SdE-20	20–25	3.79	7.6	-27.13	68.8	4.8	14.4	1.89	8.17	6.8	70.8	5.97	5.68	6.29	361	1.30
Location 2 (FGA)																
R2-P1-P1																
SdE-61	0–5	3.97	5.1	-28.81	69.0	4.9	14.1	0.95	3.27	18.5	15.2	2.58	1.54	4.46	584	0.73
SdE-62	5–10	3.82	5.4	-28.12	68.4	5.2	13.1	1.06	5.30	3.4	44.9	3.71	2.51	5.81	447	0.91
SdE-63	10–15	3.83	6.1	-27.64	68.3	5.3	12.9	1.45	4.69	4.0	123.0	3.80	3.09	7.00	331	0.67
SdE-64	15–20	3.91	6.2	-27.46	73.2	5.8	12.6	1.80	5.47	5.2	108.3	4.54	3.44	6.29	309	0.87
SdE-65	20–25	3.94	5.9	-27.42	61.5	4.8	12.8	2.20	2.58	5.0	100.9	3.49	3.79	6.97	226	0.37
SdE-66	30–35	4.13	5.6	-27.30	70.3	5.7	12.4	3.33	3.62	12.9	358.0	5.14	5.38	5.58	402	0.65
R2-P1-P2																
SdE-67	0–5	3.83	4.8	-28.15	62.3	4.8	13.0	1.29	4.34	4.1	65.3	3.46	2.38	4.52	476	0.96
SdE-68	5–10	3.88	5.2	-28.26	62.8	4.7	13.3	1.25	4.11	4.5	55.5	3.31	2.21	5.66	543	0.73
SdE-69	10–15	3.91	7.1	-27.76	70.3	5.3	13.3	1.75	5.90	2.6	58.4	4.70	3.61	6.34	392	0.93
SdE-70	15–20	3.95	8.0	-27.52	71.4	5.3	13.5	1.96	4.85	3.4	86.5	4.39	4.51	7.16	311	0.68
SdE-71	20–25	3.98	7.1	-27.44	65.5	5.0	13.2	2.34	4.40	5.3	62.0	4.54	5.12	7.45	318	0.59
SdE-72	30–35	4.12	6.1	-27.34	64.4	5.0	12.8	3.10	4.98	13.5	196.9	5.59	6.02	7.10	284	0.70
R2-P2-P1																
SdE-73	0–5	3.79	6.1	-28.63	60.6	4.7	13.0	1.05	4.10	5.7	26.5	3.10	2.41	6.55	467	0.63
SdE-74	5–10	3.81	6.8	-28.33	64.2	5.0	13.0	1.25	4.05	5.9	39.6	3.27	2.87	6.37	317	0.64
SdE-75	10–15	3.85	7.2	-28.06	71.9	5.6	12.8	1.65	4.18	6.0	48.5	3.74	3.74	7.58	429	0.55
SdE-76	15–20	3.89	5.6	-27.83	68.1	5.4	12.6	1.72	12.35	3.5	37.9	7.90	4.39	9.11	259	1.36
SdE-77	20–25	3.94	5.3	-27.74	63.9	5.1	12.6	2.04	5.60	3.2	50.2	4.84	4.52	7.74	263	0.72
R2-P2-P2																
SdE-78	0–5	3.87	6.1	-28.60	69.0	5.4	12.8	1.10	3.74	4.7	84.8	2.97	2.95	7.60	442	0.49
SdE-79	5–10	3.89	5.5	-28.19	71.2	5.6	12.7	1.21	5.30	3.7	86.3	3.85	3.46	8.17	278	0.65
SdE-80	10–15	3.86	5.4	-28.21	65.3	5.2	12.6	0.98	5.26	4.9	96.3	3.61	3.45	6.87	449	0.77
SdE-81	15–20	3.91	4.4	-27.75	68.5	5.4	12.7	1.30	4.88	2.6	63.7	3.74	5.21	7.34	257	0.66
SdE-82	20–25	3.93	5.3	-27.78	61.2	4.9	12.6	n.d.	n.d.	0.1	57.3	0.00	4.01	6.55	195	n.a.

*measurement done with Picarro.

**measurement done with Leco® C-H-N elemental analyser.

Al_o, Fe_o, Mn_o, Si_o. Oxalate-extractable fraction.

Al_d, Fe_d, Si_d. Dithionite-extractable fraction.

n.d.: no data.

n.a.: not applicable.

± 0.014; Kelley et al., 1999, Fig. 7a). Both areas had similar and consistent ²⁴⁰Pu/²³⁹Pu signals along their depth increments. Insignificantly higher values were measured in the FGA (up to 0.202 ± 0.004). The ²³⁹⁺²⁴⁰Pu activity distribution (Fig. 7b) at all sites exponentially decreased with depth.

The total inventory of the reference site (R1) was the highest with 163.7 ± 29.7 [Bq m⁻²] and lower at the slope sites S1 and S2. In the FGA, however, the total inventory was higher at the slope sites (S3, S4; Fig. 7b) when compared to the corresponding reference site (R2). The

inventory of each reference site was used as a basis to determine the local mass redistribution rates using two models (PDM, IM; Fig. 7c). In the NGA, the individual soil profiles (Table S5) erosion rates were in the range of -267 [t km⁻² yr⁻¹] to -3655 [t km⁻² yr⁻¹] having a respectively slope angle of 10° and 20°. The FGA soils, with a slope angle of 5°, exhibited deposition rates range from 11 [t km⁻² yr⁻¹] to 510 [t km⁻² yr⁻¹], only at S3 one profile yielded soil erosion rates from -235 to -394 [t km⁻² yr⁻¹] (Table S5).

Using the percolation theory, the long-term erosion rates of the FGA and NGA were calculated as, 101–140 [t km⁻² yr⁻¹] for the NGA and

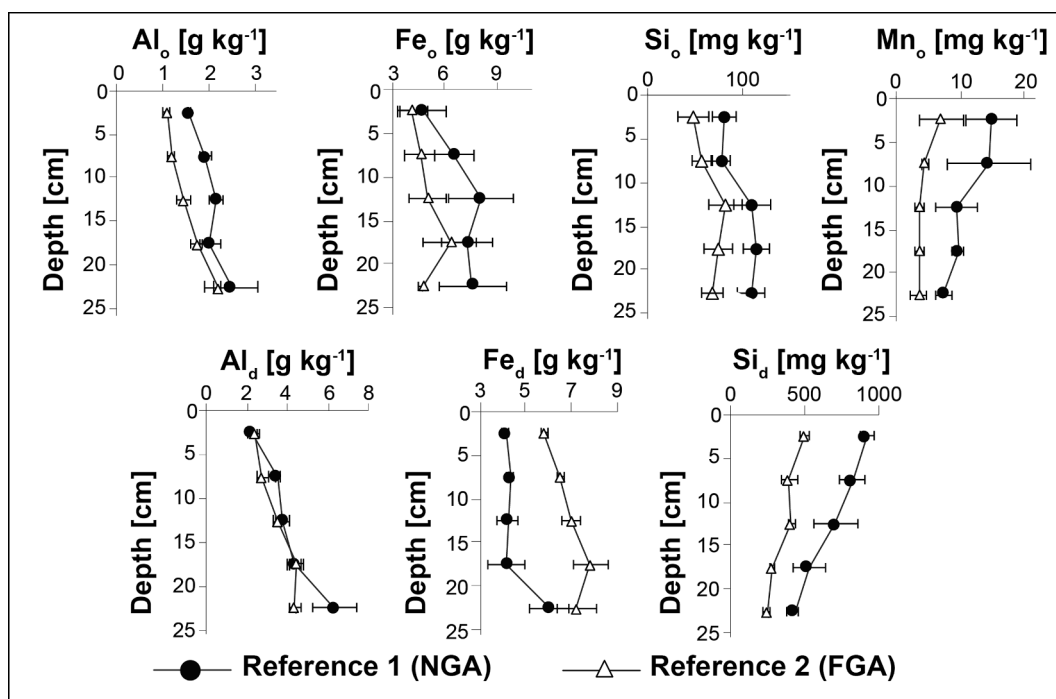


Fig. 4. Content of oxalate- and dithionite-extractable elements in the reference profiles. Values represent the average ($n = 2$) for the depth increment at each location.

176–248 [$\text{t km}^{-2} \text{yr}^{-1}$] for the FGA (Table 5). In contrast to the Pu measurements and, thus, the short-term rates, the overall and long-term erosion rates were higher at the FGA sites. Owing to the simplifications made to run the model, it was necessary to know which effect a change in these parameters had on the results (Egli et al., 2018). A convenient way to express the sensitivity of a system to changes in parameters is the normalised sensitivity coefficient, $Q_{i,m}$, given by.

$$Q_{i,m} = \frac{\partial \ln C_i}{\partial \ln P_m} \quad (5)$$

where C_i is the dependent variable and P is the value of parameter m (Furrer et al., 1990). This formula expresses a partial derivative based on the percent change in the dependent variable caused by a 1% change in the value of the parameter m . An increase in the infiltration rates and particle size diameter leads to a corresponding, linear and equivalent change in erosion rates whereas time seemed almost irrelevant (Table 6).

4.5. Surface age at FGA and ^{10}Be in the soils

The moraine boulder sample yielded $31.52 \pm 1.01 \times 10^4$ [^{10}Be atom g^{-1}] and resulted in a surface exposure age of about 22502 ± 1930 years (Table 8). This boulder deposition age marked the earliest onset of soil formation for our soil sites located on the lateral moraine surface in the FGA. The content of meteoric ^{10}Be along the soil profiles was relatively homogeneous (Fig. 8a; Table 7) and no clear depth trend pattern was recognised. Usually, an exponential decrease with depth at undisturbed sites is expected which was clearly not the case at our sites.

5. Discussion

5.1. Surface age and meteoric ^{10}Be in soils

To have a reasonable time frame for the onset of soil formation at the FGA, we have selected and sampled one of the largest, still in place appearing boulder on the adjacent lateral moraine boulder field (~1650

m a.s.l.). The deposition age of the boulder was estimated to be around 22 ka BP and seems, thus, close to the LGM. However, this boulder represented the first and only absolute age at the investigated slope and is overall younger compared to the few surface ages available. The surface exposure ages (in-situ ^{36}Cl) of four moraine boulders at Lagoa Seca (~1400 m a.s.l.) spanned from 140 ka to 30 ka (Vieira et al., 2021). Vieira (2008), indicated that the LGMSE has happened in this part of the Mediterranean region about 30–33 ka BP. Recent investigations (e.g., Vieira et al., 2021) concluded also that the end of the Last Glacial Cycle was at about 30 ka and, thus, slightly before the LGM of the European Alps (Ivy-Ochs et al., 2008) or many other parts of the world (Palacios et al., 2020). We consider the estimated boulder deposition age as reasonable at the given altitude and in context to the global climate during this time.

The soils of the FGA are less developed considering the lower carbon content or oxalate extractable elemental contents when compared to the NGA (Fig. 3a,b; Fig. 2b; Table 3). The higher weathering degree in the NGA (Fig. 5) further supports that the soils at the NGA had more time for development. Consequently, the soils of the NGA can be considered older than the soils of the FGA. The high correlation ($R^2 = 0.93$; Fig. 8b) of oxalate extractable Fe and meteoric ^{10}Be shows that ^{10}Be tightly binds to poorly crystalline Fe-phases in the soil. Other authors found that meteoric ^{10}Be can be incorporated as a cation in oxyhydroxide complexes (Barg et al. 1997; Takahashi et al. 1999). Therefore, the distribution pattern of meteoric ^{10}Be is governed to a certain extent by Fe-oxyhydroxides. The almost homogenous vertical pattern of the meteoric ^{10}Be content indicates long-term disturbances and mixing processes (as it sometimes may also be observed for *in-situ* ^{10}Be in soils; Schaller et al., 2010). Several factors, e.g., cryoturbation, bioturbation, ploughing, sheet wash/erosion and deposition may lead to such a soil mixing or soil mass redistribution. We consider ploughing to be absent in this area, because R2 is far from the traditional high elevation rye fields where ploughing was used.

5.2. Soil erosion and soil development

Under similar environmental conditions (geology, vegetation,

Table 4

Total elemental content (given in oxide form) of all soil samples. Trace element contents are presented in Table S4. LOI = loss on ignition (550 °C).

Site	Depth [cm]	Na ₂ O [%]	MgO [%]	Al ₂ O ₃ [%]	SiO ₂ [%]	P ₂ O ₅ [%]	K ₂ O [%]	CaO [%]	TiO ₂ [%]	MnO [%]	Fe ₂ O ₃ [%]	LOI [%]	Sum [%]
Location 1 (NGA)													
R1-P1-P1													
	0–5	5.31	1.05	27.9	50.6	1.40	6.51	0.86	0.52	0.02	5.86	23.2	100
	5–10	5.03	1.03	27.8	51.1	1.36	6.69	0.86	0.51	0.03	5.67	23.7	100
	10–15	4.95	1.09	30.0	48.2	1.95	6.43	0.84	0.53	0.02	6.04	18.8	100
	15–20	4.84	1.10	30.8	47.5	2.02	6.34	0.86	0.57	0.02	5.91	12.6	100
	20–25	4.47	1.05	30.6	46.7	2.31	6.88	0.89	0.67	0.02	6.44	13.7	100
R1-P1-P2													
	0–5	5.04	1.12	28.7	48.2	1.60	6.25	0.85	0.63	0.03	7.60	23.8	100
	5–10	5.16	1.11	28.2	48.7	1.81	6.53	0.93	0.61	0.03	6.92	23.4	100
	10–15	4.99	1.10	29.5	48.6	1.86	6.13	0.81	0.58	0.02	6.42	19.3	100
	15–20	5.19	1.12	30.4	46.8	2.16	6.37	0.81	0.59	0.02	6.50	16.5	100
	20–25	5.08	1.13	30.7	47.0	2.10	6.59	0.82	0.59	0.02	6.01	12.3	100
R1-P2-P1													
	0–5	5.77	1.10	27.2	51.1	1.24	6.39	0.91	0.53	0.02	5.79	27.9	100
	5–10	5.53	1.16	29.8	47.6	1.74	6.29	0.80	0.58	0.02	6.50	21.6	100
	10–15	5.15	1.09	30.1	48.1	1.86	6.27	0.78	0.61	0.02	6.08	16.5	100
	15–20	4.89	1.09	30.4	46.9	2.18	6.29	0.76	0.63	0.02	6.87	17.8	100
	20–25	4.84	1.10	32.5	44.2	2.86	6.03	0.70	0.65	0.02	7.11	19.1	100
R1-P2-P2													
	0–5	5.32	1.12	27.9	50.3	1.27	6.68	0.80	0.56	0.02	6.02	22.9	100
	5–10	5.03	1.08	29.6	48.4	1.75	6.55	0.77	0.60	0.02	6.19	16.3	100
	10–15	5.03	1.07	30.5	47.5	1.88	6.53	0.79	0.61	0.02	6.06	14.0	100
	15–20	4.87	1.10	30.6	47.1	2.21	6.56	0.75	0.62	0.02	6.14	15.0	100
	20–25	4.74	1.08	31.1	46.6	2.35	6.09	0.75	0.66	0.02	6.63	14.8	100
S1-P1-P1													
	0–5	4.79	1.02	29.0	49.9	1.22	7.41	0.77	0.58	0.02	5.34	17.3	100
	5–10	4.21	1.07	31.2	48.0	1.68	6.99	0.72	0.58	0.02	5.55	11.8	100
	10–15	4.33	1.11	31.5	46.9	1.87	6.99	0.73	0.59	0.02	5.96	12.1	100
	15–20	1.44	0.71	32.4	49.3	1.75	7.21	0.74	0.60	0.02	5.82	12.0	100
	20–25	4.37	1.07	31.2	47.9	1.47	7.24	0.71	0.55	0.02	5.48	11.0	100
S1-P1-P2													
	0–5	4.72	1.02	30.0	48.9	1.46	7.45	0.75	0.53	0.02	5.15	12.4	100
	5–10	4.48	1.05	31.6	47.4	1.68	7.20	0.75	0.50	0.02	5.36	11.8	100
	10–15	4.43	0.97	30.6	48.4	1.41	7.21	0.77	0.56	0.02	5.70	12.8	100
	15–20	4.37	1.07	32.1	47.2	1.35	7.15	0.71	0.53	0.02	5.44	11.0	100
	20–25	3.90	1.09	35.8	44.4	1.17	6.95	0.63	0.51	0.02	5.54	10.6	100
S1-P2-P1													
	0–5	7.26	1.71	25.7	49.0	1.17	6.70	2.12	0.55	0.07	5.79	58.4	100
	5–10	4.81	1.03	30.3	48.6	1.34	7.18	0.79	0.54	0.02	5.31	13.6	100
	10–15	4.77	1.06	31.3	47.8	1.26	7.02	0.82	0.54	0.02	5.40	13.1	100
	15–20	4.68	1.03	30.3	49.1	0.96	7.60	0.82	0.57	0.02	4.93	9.6	100
	20–25	4.42	1.01	30.9	48.6	0.97	7.52	0.86	0.58	0.02	5.19	8.6	100
S1-P2-P2													
	0–5	5.99	1.16	28.8	48.7	1.36	6.62	0.93	0.54	0.03	5.87	41.9	100
	5–10	4.85	0.99	29.8	49.3	1.43	7.31	0.81	0.50	0.02	4.97	13.3	100
	10–15	4.51	1.10	32.1	47.9	1.16	6.71	0.77	0.55	0.02	5.21	9.7	100
	15–20	4.44	1.02	31.6	48.0	1.16	6.84	0.80	0.60	0.02	5.50	11.4	100
	20–25	4.67	1.05	30.8	48.5	1.21	7.16	0.78	0.56	0.02	5.24	13.8	100
S2-P1-P1													
	0–5	4.00	1.20	34.1	45.3	0.95	6.93	0.69	0.59	0.03	6.22	9.4	100
	5–10	3.72	1.06	36.2	45.0	0.98	6.58	0.60	0.51	0.02	5.27	10.6	100
	10–15	2.59	1.03	40.4	42.7	1.11	6.49	0.28	0.40	0.02	5.06	14.6	100
	15–20	2.31	0.97	41.2	42.7	1.03	6.58	0.18	0.33	0.01	4.74	12.6	100
	20–25	2.25	0.94	40.7	43.4	0.91	6.84	0.16	0.32	0.01	4.46	11.6	100
S2-P1-P2													
	0–5	3.66	1.10	33.2	47.2	0.95	6.91	0.73	0.59	0.02	5.64	10.8	100
	5–10	3.28	1.01	40.4	41.7	1.11	6.14	0.54	0.47	0.02	5.38	12.0	100
	10–15	3.15	0.87	40.9	42.6	0.82	6.24	0.50	0.32	0.01	4.57	8.0	100
	15–20	2.76	0.81	45.3	40.6	0.81	4.79	0.48	0.30	0.01	4.17	14.6	100
	20–25	3.05	0.78	39.7	45.0	0.64	5.52	0.70	0.34	0.01	4.28	7.4	100
S2-P2-P1													
	0–5	4.43	1.10	34.6	45.8	0.95	6.79	0.79	0.47	0.02	5.13	9.8	100
	5–10	3.97	1.07	38.0	44.0	1.03	5.89	0.95	0.42	0.02	4.69	8.6	100
	10–15	3.82	0.72	38.2	46.1	0.69	5.98	0.91	0.25	0.01	3.34	5.4	100
	15–20	3.74	0.70	39.9	45.0	0.71	5.38	1.12	0.22	0.01	3.17	4.4	100
	20–25	3.94	0.66	39.0	46.2	0.78	5.64	1.08	0.21	0.01	2.57	5.4	100
S2-P2-P2													
	0–5	4.32	1.09	37.3	44.0	0.93	6.10	0.88	0.44	0.03	4.99	9.6	100
	5–10	4.23	0.84	35.4	47.7	0.74	5.65	1.03	0.33	0.02	4.13	4.6	100
	10–15	3.20	0.88	45.5	41.1	0.96	4.91	0.42	0.20	0.02	2.89	16.4	100
	15–20	4.20	0.74	37.1	46.6	0.69	5.49	1.24	0.31	0.02	3.54	4.8	100
	20–25	3.40	0.75	39.8	46.0	0.64	5.51	0.71	0.23	0.02	3.03	6.4	100

(continued on next page)

Table 4 (continued)

Site	Depth [cm]	Na ₂ O [%]	MgO [%]	Al ₂ O ₃ [%]	SiO ₂ [%]	P ₂ O ₅ [%]	K ₂ O [%]	CaO [%]	TiO ₂ [%]	MnO [%]	Fe ₂ O ₃ [%]	LOI [%]	Sum [%]
Location 2 (FGA)													
R2-P1-P1													
	0–5	4.25	0.89	24.8	55.7	0.71	8.50	0.38	0.46	0.02	4.26	13.8	100
	5–10	4.04	0.85	25.7	54.3	0.76	8.38	0.25	0.50	0.02	5.17	13.9	100
	10–15	4.04	0.84	26.4	53.6	0.75	8.48	0.24	0.52	0.02	5.21	13.8	100
	15–20	3.97	0.87	27.5	52.2	0.80	8.15	0.24	0.52	0.02	5.78	15.2	100
	20–25	4.26	0.84	27.1	52.3	0.74	8.44	0.22	0.50	0.02	5.59	13.4	100
	30–35	4.48	0.93	30.5	48.6	0.99	7.99	0.22	0.50	0.02	5.73	15.1	100
R2-P1-P2													
	0–5	3.82	0.86	25.8	54.8	0.73	8.43	0.23	0.50	0.02	4.83	12.3	100
	5–10	4.03	0.89	26.4	53.4	0.77	8.52	0.25	0.51	0.02	5.21	13.2	100
	10–15	4.05	0.83	26.3	53.6	0.76	8.59	0.24	0.49	0.02	5.17	13.8	100
	15–20	4.19	0.86	27.3	52.2	0.77	8.46	0.23	0.51	0.02	5.54	13.9	100
	20–25	4.16	0.91	28.0	51.8	0.78	8.14	0.21	0.50	0.02	5.48	14.9	100
	30–35	4.16	0.95	30.0	49.3	0.90	7.97	0.23	0.51	0.02	6.04	14.7	100
R2-P2-P1													
	0–5	4.11	0.89	25.8	54.5	0.63	8.40	0.21	0.51	0.02	5.02	12.8	100
	5–10	3.85	0.82	25.7	54.7	0.65	8.35	0.19	0.49	0.02	5.28	14.3	100
	10–15	4.34	0.88	26.5	53.0	0.72	8.06	0.19	0.53	0.02	5.74	15.2	100
	15–20	4.15	0.90	27.1	52.4	0.72	8.17	0.19	0.53	0.02	5.87	14.4	100
	20–25	4.15	0.87	27.9	51.5	0.74	8.20	0.19	0.55	0.02	5.85	13.8	100
R2-P2-P2													
	0–5	3.71	0.95	26.4	53.5	0.69	8.32	0.22	0.54	0.02	5.73	14.3	100
	5–10	3.98	0.87	26.3	53.4	0.71	8.26	0.20	0.52	0.02	5.72	15.4	100
	10–15	3.99	0.89	26.3	53.6	0.69	8.39	0.19	0.50	0.02	5.44	15.4	100
	15–20	3.97	0.87	26.7	53.2	0.70	8.02	0.19	0.51	0.02	5.86	15.8	100
	20–25	3.88	0.88	27.2	52.6	0.75	8.16	0.19	0.51	0.02	5.82	13.5	100
S3-P1-P1													
	0–5	3.74	0.85	26.0	54.6	0.99	8.57	0.24	0.45	0.02	4.61	13.9	100
	5–10	3.33	0.80	27.0	55.1	0.92	7.86	0.18	0.42	0.02	4.36	13.7	100
	10–15	4.20	0.89	26.9	53.1	0.92	8.35	0.21	0.47	0.02	4.98	13.7	100
	15–20	3.79	0.88	27.8	52.4	0.89	8.34	0.20	0.48	0.02	5.21	13.6	100
	20–25	3.96	0.88	27.8	52.4	0.86	8.36	0.20	0.45	0.02	5.11	14.6	100
S3-P1-P2													
	0–5	4.07	0.76	23.4	57.8	0.80	8.62	0.23	0.38	0.02	3.94	13.9	100
	5–10	4.15	0.69	23.2	58.1	0.70	8.69	0.20	0.38	0.01	3.88	12.7	100
	10–15	3.84	0.83	26.0	54.7	0.91	8.43	0.20	0.45	0.02	4.72	13.7	100
	15–20	3.85	0.82	26.1	54.5	0.87	8.52	0.21	0.43	0.02	4.65	13.0	100
	20–25	3.93	0.87	27.3	53.1	0.84	8.49	0.20	0.45	0.02	4.84	13.0	100
S3-P2-P1													
	0–5	4.20	0.83	24.7	55.7	0.94	8.47	0.23	0.42	0.02	4.50	15.4	100
	5–10	4.34	0.83	24.9	55.0	1.11	8.32	0.24	0.45	0.02	4.79	14.5	100
	10–15	4.31	0.86	25.7	53.6	1.13	8.38	0.21	0.48	0.02	5.24	15.2	100
	15–20	4.56	0.84	26.8	52.6	1.01	8.23	0.23	0.46	0.02	5.35	15.0	100
	20–25	4.40	0.91	28.9	49.2	1.11	8.03	0.22	0.53	0.02	6.62	16.3	100
S3-P2-P2													
	0–5	3.67	0.81	24.3	57.0	0.96	8.53	0.23	0.42	0.02	4.15	13.8	100
	5–10	4.05	0.83	25.0	54.9	1.20	8.42	0.22	0.46	0.02	4.90	14.5	100
	10–15	3.83	0.79	24.4	55.9	1.14	8.47	0.21	0.42	0.02	4.80	14.8	100
	15–20	4.06	0.76	24.6	55.6	1.00	8.25	0.20	0.39	0.02	5.08	15.2	100
	20–25	4.13	0.80	27.0	53.0	1.18	7.98	0.21	0.41	0.02	5.25	15.7	100
S4-P1-P1													
	0–5	3.78	0.55	20.3	62.2	0.42	8.81	0.21	0.35	0.01	3.46	12.6	100
	5–10	3.77	0.73	23.0	58.3	0.58	9.04	0.22	0.42	0.01	3.96	10.8	100
	10–15	3.84	0.70	22.8	58.7	0.55	8.74	0.19	0.38	0.01	4.12	11.9	100
	15–20	4.03	0.66	22.6	58.7	0.48	8.76	0.18	0.37	0.01	4.20	11.9	100
	20–25	3.63	0.63	22.8	59.1	0.47	8.71	0.17	0.36	0.01	4.08	11.8	100
	30–35	4.20	0.89	29.3	50.2	0.83	8.55	0.20	0.49	0.02	5.39	11.0	100
S4-P1-P2													
	0–5	4.00	0.73	22.4	59.1	0.59	9.12	0.23	0.35	0.01	3.41	10.9	100
	5–10	3.86	0.73	23.3	58.2	0.60	8.88	0.21	0.40	0.01	3.82	11.3	100
	10–15	3.86	0.86	25.7	54.4	0.70	8.86	0.22	0.48	0.02	4.94	11.8	100
	15–20	4.06	0.87	26.3	53.8	0.72	8.65	0.21	0.46	0.02	4.87	11.9	100
	20–25	3.82	0.76	25.5	55.5	0.63	8.68	0.18	0.42	0.01	4.49	11.2	100
S4-P2-P1													
	0–5	3.98	0.87	23.9	57.1	0.73	8.45	0.23	0.47	0.02	4.27	13.9	100
	5–10	3.81	0.70	22.1	59.5	0.68	8.75	0.20	0.39	0.01	3.90	12.8	100
	10–15	4.04	0.75	24.2	56.5	0.73	8.85	0.20	0.44	0.01	4.27	12.2	100
	15–20	3.92	0.81	25.7	54.6	0.78	8.69	0.19	0.47	0.01	4.87	13.4	100
	20–25	3.97	0.86	26.4	53.6	0.77	8.62	0.19	0.49	0.01	5.13	13.4	100
S4-P2-P2													
	0–5	3.55	0.74	22.7	59.0	0.76	8.65	0.23	0.41	0.01	3.90	13.0	100
	5–10	4.05	0.84	25.6	54.4	0.95	8.43	0.21	0.50	0.02	4.99	13.4	100
	10–15	3.80	0.76	24.3	56.6	0.79	8.67	0.19	0.45	0.01	4.42	12.9	100
	15–20	4.08	0.83	25.7	54.2	0.77	8.57	0.19	0.49	0.01	5.13	14.3	100
	20–25	3.86	0.82	27.0	52.8	0.82	8.80	0.18	0.49	0.01	5.22	11.3	100

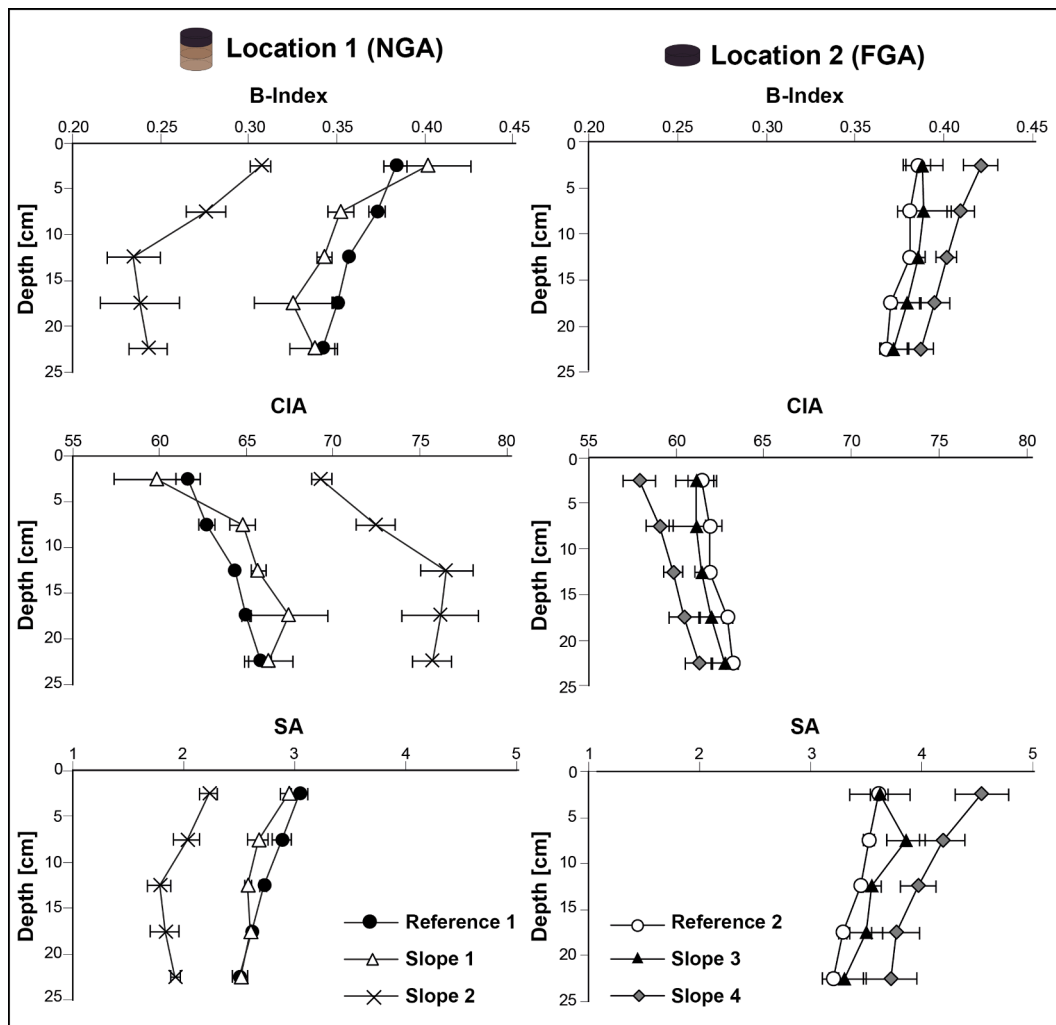


Fig. 5. Weathering indices along the soil profiles at the reference and slope sites of the two landscape settings (formerly glaciated and non-glaciated). The y-axis represents the soil depth in [cm], the x-axis the average ($n = 4$) of the elemental ratio (Table S1). Index B (Kronberg and Nesbitt, 1981), CIA = chemical index of alteration (Nesbitt and Young, 1982); SA = Silica-aluminium ratio (Ruxton, 1968).

climate, topography), soil formation is merely a function of soil erosion and soil age as time determines the mineral weathering capacity and therefore the maximum soil production rate (see section 1). Considering the calculated and estimated soil age span the expected soil formation rates after ~ 20 ka would be about 50 [$t\ km^{-2}\ yr^{-1}$] and after ~ 30 ka around 40 [$t\ km^{-2}\ yr^{-1}$] for alpine or Mediterranean areas (Raab et al., 2018). Assuming no erosion, then soil production rates (that would in this case correspond to soil formation) would be 42 [$t\ km^{-2}\ yr^{-1}$] after 30 ka and 21 [$t\ km^{-2}\ yr^{-1}$] for the NGA when using the percolation theory (Table 5). Because present-day erosion rates were in some cases very high (site S1 and S2), soil production rates must have been higher to cope with this intensity of erosion. Although the overall soil formation rates might have been low, the soils in the Estrela region remain very dynamic.

The short-term erosion rates were about 850 [$t\ km^{-2}\ yr^{-1}$] (PDM approach) in the NGA. The values obtained from the IM method were between 900 and 2100 [$t\ km^{-2}\ yr^{-1}$], a value-range that is very high even for intensively used agricultural soils (Ferreira et al., 2015). It therefore might be questioned if the IM model yields correct results. At the FGA, almost no erosion and predominately soil deposition (average ~ 230 [$t\ km^{-2}\ yr^{-1}$]) were obtained (Fig. 7c; Table S5). Since the FGA sample locations were selected at the upper part of the lateral moraine (Fig. 1c), depositions from higher elevations seem of minor importance. This trend of high erosion rates at the NGA and deposition rates at the

FGA did not correspond to the expectancies (Portes et al., 2018), since the older sites should have had a higher surface stability than the younger sites (Musso et al., 2020). Yet, the modern soil erosion rates correspond to the general accepted increase in soil erosion with increasing surface angle (Fig. 7c). Thus, the soil redistribution differences among the two study locations were also controlled by the different soil pit surface inclinations (NGA: 10° – 20° ; FGA: $\sim 5^{\circ}$), despite having a similar overall slope angle (NGA: 2° – 5° ; FGA: 3° – 7°). In contrast, the apparent depositional FGA had only about half the soil skeleton content (Table 2). A higher gravel content reduces the proportion of fine earth that is prone to erosion. The differences in grain size distribution (fine earth) among FGA and NGA are, however, relatively low (average sand: 26.6 vs 33.3% , silt: 31.9 vs. 31.7% and clay: 40.6 vs 34.4%). The profile S2 (NGA) had only patches of grassland cover which increases soil redistribution. These vegetation patches seem to be caused by former grazing giving rise to a higher soil erosion susceptibility. The pH conditions were slightly more acidic at NGA but overall comparable among the two end-member sites. The pH-depth trend at the site 'S2' shows only a weak or no increase which might be indicative of soil erosion/deposition.

If, however, the erosion rates are integrated over millennia using the percolation theory, then the general trend fits the expectancies with lower rates at the NGA compared to the FGA. The erosion rates are still rather high for natural soils (with 128 – 184 [$t\ km^{-2}\ yr^{-1}$] for the NGA

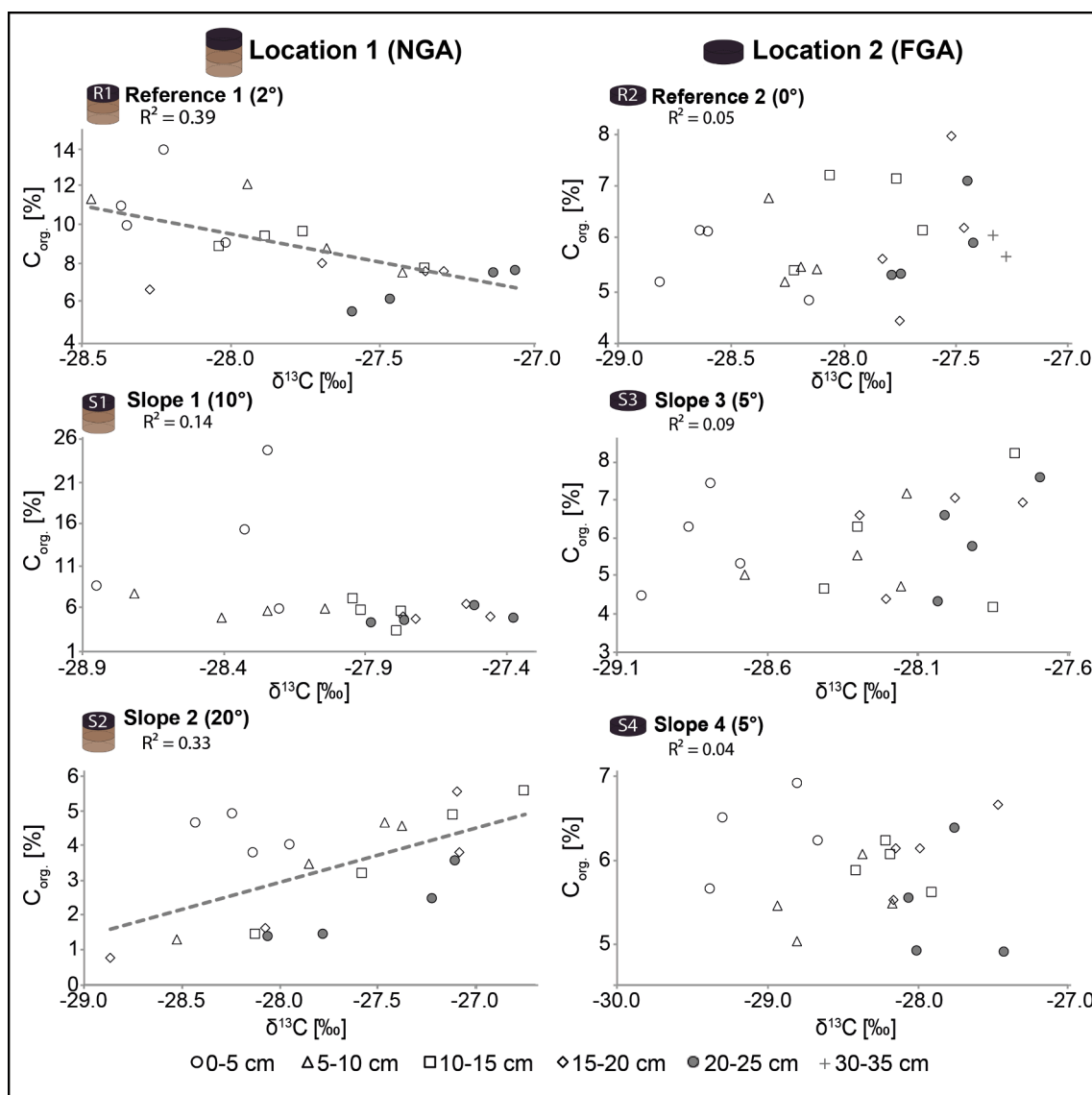


Fig. 6. Correlation between the organic carbon content ($C_{org} = C_{tot}$) and $\delta^{13}C$ signature as indicator of soil disturbance/stability (the values are given in Table S3).

and $167\text{--}236$ [$t\ km^{-2}\ yr^{-1}$] for the FGA), but they also include disturbances owing to human impact that particularly in the Mediterranean area has persisted for millennia. Due to the high erosion rates, soil production is almost identical and, thus a quasi-steady situation is reached earlier. In rapidly eroding landscapes, a steady state regarding soil thickness is reached faster than in slowly eroding soils (Ferrier and Kirchner, 2008; Norton and von Blanckenburg, 2010). The importance of erosion in the Mediterranean area is related to the long history of human activity in a region characterised by low levels of annual precipitation, the occurrence of intense rainstorms, a dry-summer season or long-lasting droughts, high evapotranspiration, the presence of steep ($>20^\circ$) slopes and the occurrence of recent tectonic activity, together with the recurrent use of fire, overgrazing and farming (García-Ruiz et al., 2013).

The comparison of long-term and short-term soil redistribution rates clearly indicates that a strong increase in erosion must have taken place due to human impact (cattle, grazing, bushfires) (Jansen et al., 2013). This is also supported in the Estrela region by the pollen analysis data from the Charco da Candieira cores, showing that the natural climatic signal in the sedimentary record diminished about 6.4 ka BP and particularly about 3.4 ka BP (Van der Knaap and Van Leeuwen, 1995, 1997) when human impact on the landscape started to prevail.

Due to the rather high erosion rates, the rate of soil production should be even higher so that soils are still being formed. Overall, the ~ 30 ka old FGA soils exhibit redistribution rates typical of much younger soils; i.e., having an age of about 5 ka (Table 5; see Fig. 8 in Egli et al., 2018). The older soils of the NGA show the reactivity of soils of alpine to Mediterranean climates (Egli et al., 2018), which have an age of approx. 8 ka (instead of about 120 ka). With increasing denudation or erosion, the chemical weathering and, thus, soil production increase (Dixon and von Blanckenburg, 2012) up to a poorly defined limit (Larsen et al., 2014; Egli et al., 2018). Erosion therefore continuously rejuvenates the soils and keeps the rate of soil production at a high level. However, soil thickness remains low. Soils having an age of 30–120 kyr normally have production rates in the range of 20–50 [$t\ km^{-2}\ yr^{-1}$] (Alewell et al., 2015). Alewell et al. (2015) showed that (tolerable) soil erosion rates must be less than or equal to the soil production rates, otherwise the soils start to degrade.

5.3. Soil stability evolution

Fallout radionuclides integrate mass movement for the last ~ 6 decades, carbon isotopes cover a time of up to a century to even millennia and cosmogenic nuclides inherit information for millennia and often

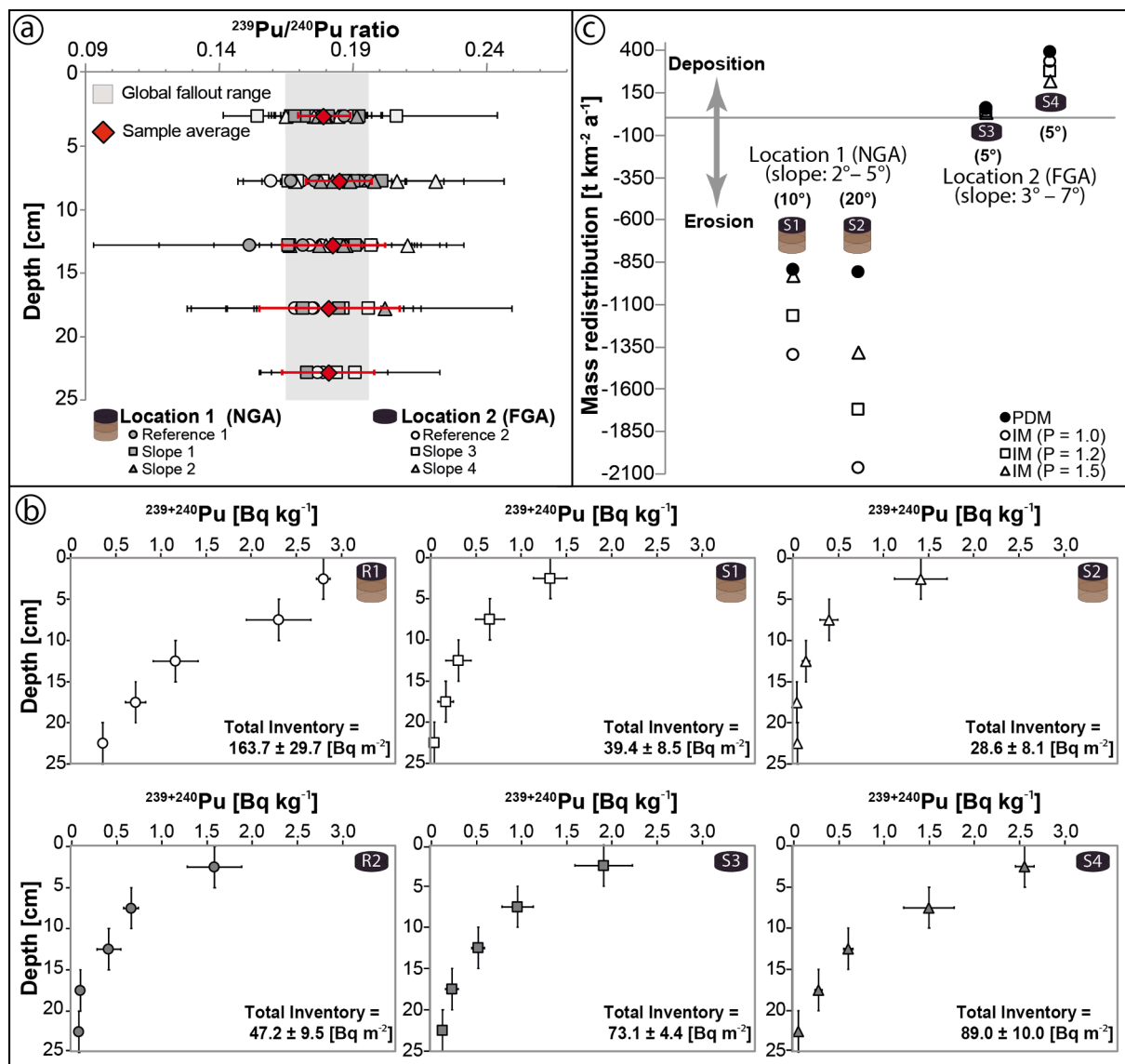


Fig. 7. (a) $^{240}\text{Pu}/^{239}\text{Pu}$ ratios and standard error of the soil samples as a function of soil depth. The average for each depth increment is given in red. The grey area indicates the global fallout range (0.180 ± 0.014) of the northern hemisphere (Kelley et al., 1999). (b) Depth-activity profiles (\pm standard error) of the investigated sites. (c) Calculated annual average soil redistribution for both reference sites using different particle size correction factors ($P = 1.0, 1.2, 1.5$) for the inventory method (IM; Lal et al., 2013) together with results of the profile distribution model (PDM; Walling and He, 1999; Zhang et al., 1990). Detailed values of the individual soil profile are given in Table S5.

Table 5

Modelled erosion rates in response to the type of site and commonly measured soil depths (40 to 60 cm). In addition, soil depth is calculated for the situation if no erosion had occurred. sP = soil production, sDE = soil depth, FGA = formerly glaciated area; NGA = non glaciated area.

Site	Profile name	sP (m yr ⁻¹)	sDE (Model) [m]	Erosion (m yr ⁻¹)	Erosion (t ha ⁻¹ yr ⁻¹)
Assuming no erosion					
Estrela	FGA	0.000062	2.56	0	0
Estrela	NGA	0.000024	4.57	0	0
Soil depth 40 cm					
Estrela	FGA	0.000300	0.42	0.000310	248
Estrela	NGA	0.000200	0.41	0.000200	140
Soil depth 60 cm					
Estrela	FGA	0.000220	0.60	0.000220	176
Estrela	NGA	0.000144	0.60	0.000144	101

Table 6

Normalized sensitivity coefficients in response to the site type. FGA = formerly glaciated area; NGA = non glaciated area.

Type of sites	Parameter	Sensitivity	
		Soil depth	Soil erosion
FGA	Particle size (d_{50})	1.010	-0.124
	Infiltration rate I	1.011	-0.142
	Time	0.000	0.000
NGA	Particle size (d_{50})	1.010	-0.041
	Infiltration rate I	1.012	-0.048
	Time	0.000	0.000

since start of soil formation. In general, meteoric ^{10}Be and $^{239+240}\text{Pu}$ are expected to decrease exponentially with depth in an undisturbed soil profile. The fallout radionuclides $^{239+240}\text{Pu}$ follow this expected trend (Fig. 7b) well. Thus, the soil column appears to be unmixed since at least the start of the deposition of plutonium isotopes in the 1960s. In

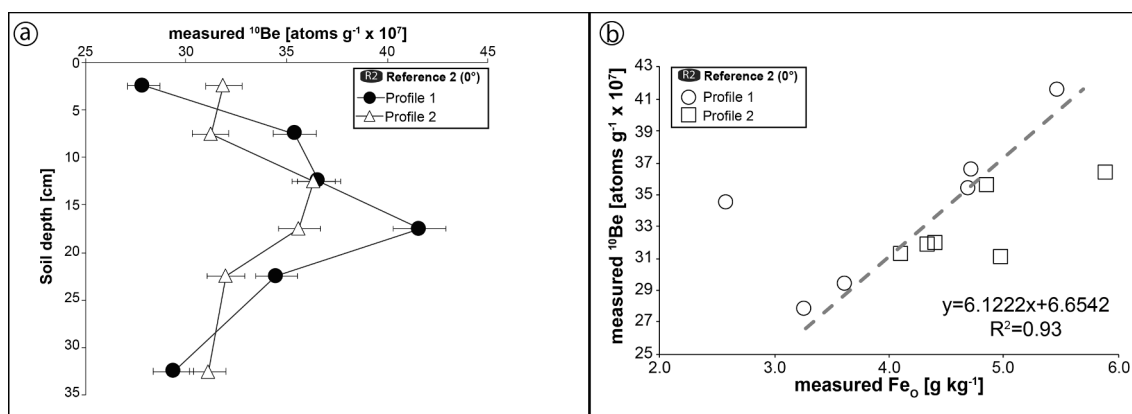


Fig. 8. (a) Meteoric ^{10}Be depth distribution in the two reference profiles at the formerly glaciated area (FGA; R2). The horizontal bars indicate the standard deviation (Table 7). (b) The correlation ($R^2 = 0.93$) of measured meteoric ^{10}Be and oxalate-extractable Fe (Fe_O ; Table 3) is supported by a p -value of 0.044.

Table 7

Meteoritic ^{10}Be measurements at the formerly glaciated area (FGA) – location 2.

Sample #	Depth [cm]	Soil mass [g]	^9Be carrier mass [mg]	$^{10}\text{Be}/^9\text{Be}$ (10^{-12}) [-]	Abs. error (10^{-12}) [-]	Error (10^{-12}) (%)	^{10}Be measured [E + 4 at g^{-1}]	Abs. error [-]	$^{10}\text{Be}/^9\text{Be}$ corrected (10^{-12}) [-]	Abs. error (10^{-12}) [E + 4 at g^{-1}]	^{10}Be corrected [%]	Abs. error [-]	Error
Location 2 (FGA)													
R2-P1-P1													
SdE-61	0–5	2.02	1.012	8.335	0.125	1.5	27,918	428	8.322	0.243	27,873	814	2.9
SdE-62	5–10	2.02	1.011	10.622	0.181	1.7	35,454	606	10.609	0.321	35,409	1072	3.0
SdE-63	10–15	2.01	1.011	10.913	0.164	1.5	36,627	549	10.900	0.318	36,583	1068	2.9
SdE-64	15–20	2.02	1.011	12.419	0.224	1.8	41,639	768	12.406	0.383	41,595	1283	3.1
SdE-65	20–25	2.01	1.013	10.228	0.174	1.7	34,514	576	10.215	0.309	34,471	1043	3.0
SdE-66	30–35	2.01	1.012	8.737	0.192	2.2	29,411	660	8.724	0.291	29,367	979	3.3
R2-P1-P2													
SdE-67	0–5	2.01	1.012	9.479	0.142	1.5	31,918	479	9.466	0.276	31,874	931	2.9
SdE-68	5–10	2.02	1.012	9.342	0.140	1.5	31,260	469	9.329	0.272	31,215	911	2.9
SdE-69	10–15	2.01	1.012	10.829	0.162	1.5	36,367	546	10.816	0.316	36,323	1060	2.9
SdE-70	15–20	2.01	1.013	10.563	0.158	1.5	35,664	535	10.550	0.308	35,620	1040	2.9
SdE-71	20–25	2.01	1.013	9.492	0.142	1.5	32,029	480	9.479	0.277	31,986	934	2.9
SdE-72	30–35	2.01	1.012	9.240	0.139	1.5	31,124	467	9.227	0.269	31,080	907	2.9

Table 8

In-situ ^{10}Be measurement at the formerly glaciated area (FGA) – location 2.

Sample	Latitude [°N]	Longitude [°W]	Elevation [m]	Rock type [-]	Sample thickness [cm]	Dip angle [°]	Dip direction [°]	Shielding factor [-]	^{10}Be content [E + 4 at g^{-1}]	error [%]	Exposure age* for different rock erosion rates		
											0 [mm ka^{-1}]	1 [mm ka^{-1}]	2 [mm ka^{-1}]
Boulder 1	40.3804	7.5943	1649	Granite	1.5	15	260	0.997572	31.52 ± 1.01	3.2	22502 ± 1930	22502 ± 1930	23382 ± 2086

* after Stone (2000).

contrast, meteoric ^{10}Be does not show a decreasing trend with soil depth (Fig. 8a). Redistribution of ^{10}Be is driven by chemical (e.g., oxides, pH) and physical (e.g., bioturbation) translocation mechanism in the soil. The acidic soil conditions ($\text{pH} < 4$; Fig. 3a,b), however, make any chemical downward translocation by clay particles unlikely (see review of Quénard et al., 2011) because the Al-concentrations are too high in the soil solution giving rise to clay aggregates (flocculation). Due to the acidic conditions and the rock type (granite), a clay translocation phase would have existed, if ever, very briefly during soil evolution. Chemical leaching is possible but not to a degree that a uniform depth trend is the consequence (Willenbring and von Blanckenburg, 2010; Boschi and Willenbring, 2021). Therefore, the redistribution of ^{10}Be across the profile must have been primarily caused by physical mechanisms. We consider meteoric ^{10}Be as an indicator of past soil disturbances (e.g., cryoturbation, bioturbation). In contrast, the carbon isotope signal

($\delta^{13}\text{C}$) of the FGA has a clear decreasing depth trend (Fig. 3b), while the signal at the NGA has a broader range with depth (Fig. 3a). However, the overall soil stability appears to be greater at the NGA, since the $\text{C}_{\text{Org}} - \delta^{13}\text{C}$ correlation is three- to ten-fold higher (Fig. 6).

We hypothesise the following timeline of soil stability since the accumulation of cosmogenic nuclides (Fig. 9): Once the soils of the FGA were able to form on the lateral moraine surface (~22 to 30 ka ago), the corresponding soil production rates were very high (up to 3000 $\text{t km}^{-2} \text{yr}^{-1}$ are commonly reported values for very young soils; Raab et al., 2018). With time, these rates strongly decreased to about 167–236 $\text{t km}^{-2} \text{yr}^{-1}$ (Table 5; Fig. 9). As previously mentioned, these rates are relatively high and would rather correspond to soils having an age of about 8 ka. The soils, however, continued to endure cryoturbation (freeze–thaw mechanism), after deglaciation. This seasonal freeze–thaw stress probably has persisted over a long-term period (multi-millennia)

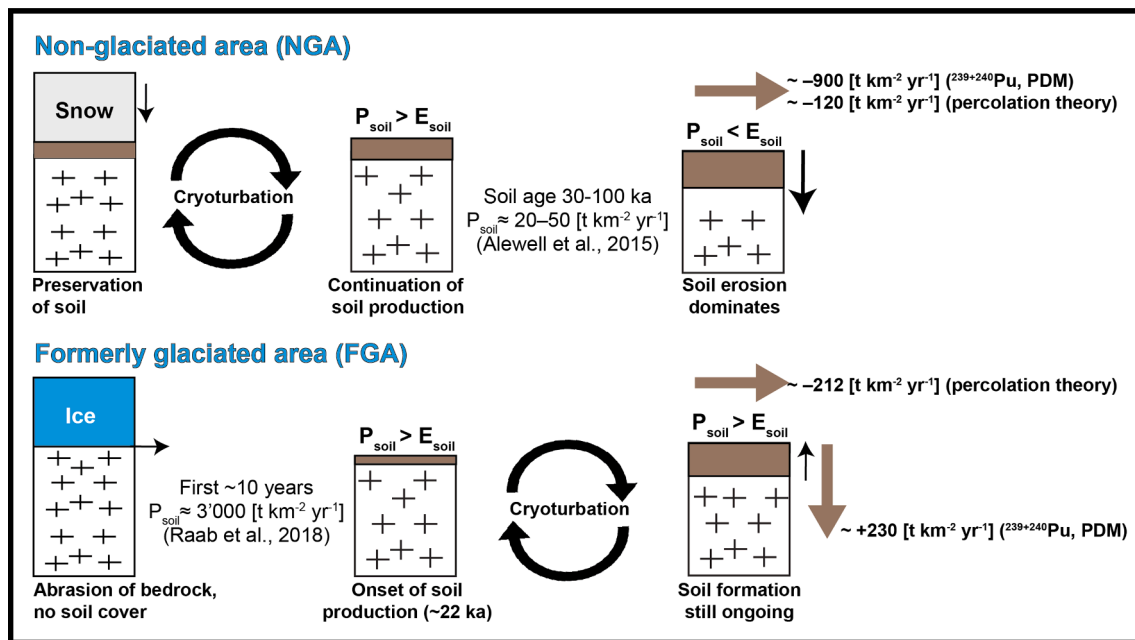


Fig. 9. Soil erosion and accumulation rates at the moraine study site (formerly glaciated area, FGA) and non-glaciated area (NGA). The investigated FGA is still under soil formation conditions due to higher soil production rates (P_{soil}). In contrast, the NGA is dominated by soil erosion (E_{soil}).

causing a disturbance of the ^{10}Be and the $\delta^{13}C$ distribution at the FGA.

The NGA soils still have a high soil production rate with $128-184 [t km^{-2} yr^{-1}]$. Typically, the rates should be $20-50 [t km^{-2} yr^{-1}]$, as previously mentioned (Alewell et al., 2015), but due to the quite strong erosion the soil production rates are kept at a relatively high level. The NGA soils seem to have been impacted for a shorter period with cryoturbation, probably during periglacial conditions (Pleistocene cold periods) since they are positioned just at a 160 m lower altitude (1495 vs 1655 m a.s.l.). Disturbances of the $\delta^{13}C$ distribution by cryoturbation is common in alpine areas (Zollinger, 2015) and has been hypothesised for other formerly glaciated areas (e.g., Portes et al., 2018). An exact time interval since the cease of cryoturbation at this altitude cannot be determined with the current data set. However, we suggest that cryoturbation has been less intensive or even absent for the last few decades (i.e., $^{239+240}Pu$ stability; Fig. 7b) in soils below an altitude of 1655 m a.s.l. at the Serra da Estrela. Vieira et al. (2003) and Vieira (2004) have shown that under the present-day climate only very shallow freezing occurs at 1650 m a.s.l. and affects only the most upper part of the soil.

6. Conclusions

Old landscape surfaces are expected to be close to an equilibrium state as soil erosion and production rates typically should decrease with increasing soil age. The quantification of these processes as a function of surface age however remains a challenge and mostly only qualitative information exists. Due to human impact or changes in the environmental conditions, short-term processes may distinctly overprint the longer-term erosion signal to the point that it is almost impossible to clearly distinguish time-dependent rates. Consequently, the disentanglement of soil erosional processes over time remains difficult. Only by using a multi-method approach, the identification and quantification of the variability of these rates over time was possible. Two end-member sites (young vs old soils) at the Serra da Estrela were compared.

Soil formation started about 22 to 30 ka ago in the formerly glaciated area (FGA). Soils at the FGA have a lower degree of weathering and lower carbon compared to soils in the non-glaciated area (NGA). In contrast to our hypothesis (i), the older soils at the NGA have a higher present-day erosion rate than the younger FGA soils, probably due to the higher grazing impact and, thus, loss of vegetation cover. Under such

conditions, local higher slopes also contribute to an increased soil erosion rate. Thus, the NGA is in a disequilibrium with respect to soil erosion and soil production over the last few decades. However, over a millennium timescale, the soil redistribution rates at the FGA are higher than at the NGA and align with expected higher geomorphic dynamics at the younger FGA soil surface. Therefore, the isotope specific observation periods of the short ($^{239+240}Pu$) and long-term (^{10}Be) soil redistribution indicators revealed contrasting soil dynamics for the two sites due to a changed geomorphic situation over time and the recent land use impact.

With respect to hypothesis (ii), no indication of vegetation degradation was found at the NGA. However, the effect of grazing or bush-fires, and thus human impact, has distinctly increased and accelerated soil erosion rates at the NGA in the recent past. The formerly glaciated areas are usually at the highest altitudes and thus less impacted by human activity. The anthropogenically-induced processes now dictate the high landscape dynamics in Mediterranean mountain areas.

The combination of isotope techniques ($^{239+240}Pu$, $\delta^{13}C$, ^{10}Be) and the application of the percolation theory provided an additional qualitative assessment about past soil mixing processes over different time periods. At an altitude of ~ 1650 m a.s.l., the FGA has experienced soil mixing, probably by freeze-thaw cycles (cryoturbation) over many millennia since deglaciation. The NGA at ~ 1500 m a.s.l. seems to have been influenced either during periglacial conditions or within the first few millennia after deglaciation. During the last few decades, cryoturbation seems to have been less active.

Overall, our multi-method approach provides insight into the temporal evolution of surface processes. The utility of cosmogenic nuclide analysis and applications gives rise to major advances in our understanding of surface erosion. Future work should utilise paired nuclides such as in-situ ^{14}C - ^{10}Be , which is a highly sensitive chronometer for quantifying sediment production, transport, and storage over 10^2-10^4 yr timescales, and may be suitable to detect more subtle erosional or soil burial phases.

Declaration of Competing Interest

The authors declare that they have no known competing financial interests or personal relationships that could have appeared to influence the work reported in this paper.

Acknowledgement

This research was supported by the Forschungskredit of the University of Zürich FK-19-108. Additional funds were provided by the Stiftung für Wissenschaftliche Forschung of the University of Zürich, grant no. STWF-20-02. Gerald Raab was supported by the Early Postdoc. Mobility Fellowship P2ZHP2_199662. The Estrela UNESCO Global Geopark is thanked for logistical support to field work. Furthermore, we thank the anonymous reviewers for their suggestions and comments on an earlier version of the manuscript.

Appendix A. Supplementary material

Supplementary data to this article can be found online at <https://doi.org/10.1016/j.catena.2022.106314>.

References

- Alewel, C., Egli, M., Meusbürger, K., 2015. An attempt to estimate tolerable soil erosion rates by matching soil formation with denudation in Alpine grasslands. *J. Soils Sediments* 15 (6), 1383–1399.
- Balco, G., Stone, J.O., Lifton, N.A., Dunai, T.J., 2008. A complete and easily accessible means of calculating surface exposure ages or erosion rates from ^{10}Be and ^{26}Al measurements. *Quat. Geochronol.* 3 (3), 174–195. <https://doi.org/10.1016/j.quageo.2007.12.001>.
- Barg, E., Lal, D., Pavich, M.J., Caffee, M.W., Southon, J.R., 1997. Beryllium geochemistry in soils: evaluation of $^{10}\text{Be}/^{9}\text{Be}$ ratios in authigenic minerals as a basis for age models. *Chem. Geol.* 140 (3–4), 237–258. [https://doi.org/10.1016/S0009-2541\(97\)00051-X](https://doi.org/10.1016/S0009-2541(97)00051-X).
- Beckhoff, B., Kanngießner, B., Langhoff, N., Wedell, R., Wolff, H., 2006. *Handbook of Practical X-ray Fluorescence Analysis*. Springer, Berlin.
- Bellin, N., Vanacker, V., De Baets, S., 2013. Anthropogenic and climatic impact on Holocene sediment dynamics in SE Spain: a review. *Quat. Int.* 308–309, 112–129.
- Boschi, V., Willenbring, J.K., 2021. Chemical and physical drivers of beryllium retention in two soil endmembers. *Sci. Total Environ.* 754, 141591. <https://doi.org/10.1016/j.scitotenv.2020.141591>.
- Brown, E.T., Edmond, J.M., Raisbeck, G.M., Yiou, F., Desgarceaux, S., 1992. Effective attenuation length of cosmic rays producing ^{10}Be and ^{26}Al in quartz: Implications for surface exposure dating. *Geophys. Res. Lett.* 9, 369–372. <https://doi.org/10.1029/92GL00266>.
- Cammeraat, L.H., Imeson, A.C., 1998. Deriving indicators of soil degradation from soil aggregation studies in southeastern Spain and southern France. *Geomorphology* 23 (2–4), 307–321.
- Chmieleff, J., von Blanckenburg, F., Kossert, K., Jakob, D., 2010. Determination of the ^{10}Be half-life by multicollector ICP-MS and liquid scintillation counting. *Nuclear Instruments Methods Phys. Res. Sect. B: Beam Interaction Mater. Atoms* 268 (2), 192–199. <https://doi.org/10.1016/j.nimb.2009.09.012>.
- Christl, M., Vockenhuber, C., Kubik, P.Q., Wacker, L., Lachner, J., Alfimov, V., Synal, H. A., 2013. The ETH Zurich AMS facilities: Performance parameters and reference materials. *Nuclear Instruments Methods Phys. Res. B* 294, 29–38. <https://doi.org/10.1016/j.nimb.2012.03.004>.
- Clark, P.U., Dyke, A.S., Shakun, J.D., Carlson, A.E., Clark, J., Wohlfarth, B., Mitrovica, J. X., Hostetler, S.W., McCabe, A.M., 2009. The last glacial maximum. *Science* 325 (5941), 710–714.
- Connor, S.E., Araújo, J., van der Knaap, W.O., van Leeuwen, J.F.N., 2012. A long-term perspective on biomass burning in the Serra da Estrela, Portugal. *Quat. Sci. Rev.* 55, 114–124.
- Daveau, S., 1971. La glaciation de la Serra da Estrela. *Finisterra* 6, 5–40.
- Dixon, J.L., Amundson, R., 2009. The critical role of climate and saprolite weathering in landscape evolution. *Earth Surf. Process. Landforms* 34 (11), 1507–1521.
- Dixon, J.L., von Blanckenburg, F., 2012. Soils as pacemakers and limiters of global silicate weathering. *C.R. Geosci.* 344 (11–12), 597–609.
- Egli, M., Fitze, P., Mirabella, A., 2001. Weathering and evolution of soils formed on granitic, glacial deposits: results from chronosequences of Swiss alpine environments. *Catena* 45 (1), 19–47.
- Egli, M., Dahms, D., Norton, K., 2014. Soil formation rates on silicate parent material in alpine environments: Different approaches, different results? *Geoderma* 213, 320–333.
- Egli, M., Hunt, A.G., Dahms, D., Raab, G., Derungs, C., Raimondi, S., Yu, F., 2018. Prediction of soil formation as a function of age using the percolation theory approach. *Front. Environ. Sci.* 6, 108.
- Ferrier, K.L., Kirchner, J.W., 2008. Effects of physical erosion on chemical denudation rates: A numerical modeling study of soil-mantled hillslopes. *Earth Planet. Sci. Lett.* 272 (3–4), 591–599.
- Ferreira, V., Panagopoulos, T., Cakula, A., Andrade, R., Arvela, A., 2015. Predicting soil erosion after land use changes for irrigating agriculture in a large reservoir of southern Portugal. *Agric. Agric. Sci. Procedia* 4, 40–49.
- Furrer, G., Sollins, P., Westall, J.C., 1990. The study of soil chemistry through quasi-steady-state models: II. Acidity of soil solution. *Geochim. Cosmochim. Acta* 54 (9), 2363–2374.
- García-Ruiz, J.M., Nadal-Romero, E., Lana-Renault, N., Beguería, S., 2013. Erosion in Mediterranean landscapes: changes and future challenges. *Geomorphology* 198, 20–36.
- Gosse, J.C., Phillips, F.M., 2001. Terrestrial in situ produced cosmogenic nuclides: Theory and application. *Quat. Sci. Rev.* 20, 1475–1560. [https://doi.org/10.1016/S0277-3791\(00\)00171-2](https://doi.org/10.1016/S0277-3791(00)00171-2).
- Google Earth. 2021. <http://www.earth.google.com> (access March 26, 2021).
- Harnois, L., 1988. The CIW index: a new chemical index of weathering. *Sed. Geol.* 55 (3–4), 319–322.
- Heimsath, A.M., Chadwick, O.A., Roering, J.J., Levick, S.R., 2020. Quantifying erosional equilibrium across a slowly eroding, soil mantled landscape. *Earth Surf. Proc. Land.* 45 (3), 499–510.
- Heimsath, A.M., DiBiase, R.A., Whipple, K.X., 2012. Soil production limits and the transition to bedrock-dominated landscapes. *Nat. Geosci.* 5 (3), 210–214.
- Heimsath, A.M., Fink, D., Hancock, G.R., 2009. The ‘humped’ soil production function: eroding Arnhem Land, Australia. *Earth Surf Proc Land* 34 (12), 1674–1684.
- Hughes, P.D., Gibbard, P.L., 2015. A stratigraphical basis for the Last Glacial Maximum (LGM). *Quat. Intern.* 383, 174–185.
- Hunt, A.G., Ghanbarian, B., Skinner, T.E., Ewing, R.P., 2015. Scaling of geochemical reaction rates via advective solute transport. *Chaos: An Interdisciplinary. J. Nonlinear Sci.* 25 (7), 075403. <https://doi.org/10.1063/1.4913257>.
- Ivy-Ochs, S., Kerschner, H., Reuther, A., Preusser, F., Heine, K., Maisch, M., Kubik, P., Schlüchter, C., 2008. Chronology of the last glacial cycle in the European Alps. *J. Quat. Sci.* 23, 559–573.
- IUSS Working Group WRB, 2015. World reference base for soil resources 2014. Update 2015. World Soil Resources Reports. Rome.
- Jansen, J., Castro, P., Costa, L., 2013. Economic-ecologic interactions in the Serra da Estrela, Portugal. Chapter 4. 66–90 p. In: Diemont, W.H., Heijman, W.J.M., Siepel, H., Webb, N.R. (Eds.) *Economy and ecology of heathlands*. KNNV Publishing, Zeist. 462p.
- Kelley, J.M., Bond, L.A., Beasley, T.M., 1999. Global distribution of Pu isotopes and ^{237}Np . *Sci. Total Environ.* 237–238, 483–500.
- Ketterer, M.E., Hafer, K.M., Link, C.L., Kolwaite, D., Wilson, J., Mietelski, J.W., 2004. Resolving global versus local/regional Pu sources in the environment using sector ICP-MS. *J. Anal. At. Spectrom.* 19 (2), 241–245.
- Ketterer, M.E., Zhang, J., Yamada, M., 2011. Application of transuranics as tracers and chronometers in the environment. In: Baskaran, M. (Ed.), *Handbook of environmental isotope geochemistry Advance in Isotope Geochemistry*. Heidelberg: Springer. DOI: 10.1007/978-3-642-10637-8.
- Kitchener, J.A., 1984. The froth flotation process: Past, present and future-in brief. In: Ives, K.J. (Ed.), *The scientific basis of flotation (Vol. 75) NATO ASI Series (Series E: Applied Sciences)*. Dordrecht: Springer. DOI: 10.1007/978-94-009-6926-1_2.
- Kohl, C.P., Nishiizumi, K., 1992. Chemical isolation of quartz for measurement of in-situ-produced cosmogenic nuclides. *Geochimica Cosmochimica Acta* 56 (9), 3583–3587.
- Korschinek, G., Bergmaier, A., Faestermann, T., Gerstmann, U.C., Knie, K., Rugel, G., Wallner, A., Dillmann, I., Dollinger, G., von Gostomski, C.L., Kossert, K., Maiti, M., Poutivtsev, M., Remmert, A., 2010. A new value for the half-life of ^{10}Be by heavy-ion elastic recoil detection and liquid scintillation counting. *Nuclear Instrum. Methods Phys. Res. Section B: Beam Interaction Mater. Atoms* 268 (2), 187–191.
- Kronberg, G.L., Nesbitt, H.W., 1981. Quantification of weathering of soil chemistry and soil fertility. *J. Soil Sci.* 32, 453–459.
- Kubik, P.W., Christl, M., 2010. ^{10}Be and ^{26}Al measurements at the Zurich 6 MV Tandem AMS facility. *Nuclear Instrum. Methods B* 268 (7–8), 880–883. <https://doi.org/10.1016/j.nimb.2009.10.054>.
- Lal, R., Tims, S.G., Fifield, L.K., Wasson, R.J., Howe, D., 2013. Applicability of Pu-239 as a tracer for soil erosion in the wet-dry tropics of northern Australia. *Nucl. Instrum. Methods Phys. Res., Sect. B* 294, 577–583. <https://doi.org/10.1016/j.nimb.2012.07.041>.
- Lautensach, H., 1929. Eiszeitstudien in der Serra da Estrela (Portugal). *Zeitschrift für Gletscherkunde* 17, 324–369.
- Larsen, I.J., Almond, P.C., Eger, A., Stone, J.O., Montgomery, D.R., Malcolm, B., 2014. Rapid soil production and weathering in the Southern Alps, New Zealand. *Science* 343 (6171), 637–640.
- Linton, D.L., 1955. The problem of tors. *Geographical J.* 121 (4), 470–487.
- Masarik, J., Frank, M., Schäfer, J.M., Wieler, R., 2001. Correction of in situ cosmogenic nuclide production rates for geomagnetic field intensity variations during the past 800,000 years. *Geochim. Cosmochim. Acta* 65 (17), 2995–3003.
- McKeague, J.A., Brydon, J.E., Miles, N.M., 1971. Differentiation of forms of extractable iron and aluminum in soils. *Soil Sci. Soc. Am. J.* 35 (1), 33–38.
- Mehra, O., Jackson, P., 1958. Iron oxide removal from soils and clays in a dithionite-citrate-bicarbonate system buffered with sodium. *Clays Clay Miner.* 7, 317–327.
- Migoñ, P., Vieira, G., 2014. Granite Geomorphology and Its Geological Controls, Serra da Estrela, Portugal. *Geomorphology* 226, 1–14. <https://doi.org/10.1016/j.geomorph.2014.07.027>.
- Mizota, C., Van Reeuwijk, L.P., 1989. Clay mineralogy and chemistry of soils formed in volcanic material in diverse climatic regions. Clay mineralogy and chemistry of soils formed in volcanic material in diverse climatic regions., (2).
- Mora, C., 2010. A synthetic map of the climatopes of the Serra da Estrela (Portugal). *J. Maps* 6 (1), 591–608. <https://doi.org/10.4113/jom.2010.1112>.
- Mora, C., Vieira, G., 2020. The climate of Portugal. In: Vieira G., Zêzere, J.L., Mora, C. (Eds.), *Landforms and Landscapes of Portugal*, Springer: 33–46.
- Musso, A., Ketterer, M.E., Greinwald, K., Getzner, C., Egli, M., 2020. Rapid decrease of soil erosion rates with soil formation and vegetation development in periglacial areas. *Earth Surf. Proc. Land.* 45 (12), 2824–2839. <https://doi.org/10.1002/esp.4932>.

- Nesbitt, H.W., Young, G.M., 1982. Early Proterozoic climates and plate motions inferred from major element chemistry of lutites. *Nature* 299 (5885), 715–717.
- Nishiizumi, K., Imamura, M., Caffee, M.W., Southon, J.R., Finkel, R.C., McAninch, J., 2007. Absolute calibration of ^{10}Be AMS standards. *Nucl. Instrum. Methods Phys. Res., Sect. B* 258 (2), 403–413.
- Nieuwendam, A., Vieira, G., Schaefer, C., Woronko, B., Johansson, M., 2020. Reconstructing cold climate paleoenvironments from micromorphological analysis of relict slope deposits (Serra da Estrela, Central Portugal). *Permafrost Periglac. Process.* 31 (4), 567–586. <https://doi.org/10.1002/ppp.2054>.
- Norton, K.P., von Blanckenburg, F., 2010. Silicate weathering of soil-mantled slopes in an active Alpine landscape. *Geochim. Cosmochim. Acta* 74 (18), 5243–5258.
- Oliva, M., Palacios, D., Fernández-Fernández, J.M., Rodríguez-Rodríguez, L., García-Ruiz, J.M., Andrés, N., Carrasco, R.M., Pedraza, J., Pérez-Alberti, A., Valcárcel, M., Hughes, P.D., 2019. Late Quaternary glacial phases in the Iberian Peninsula. *Earth Sci. Rev.* 192, 564–600.
- Palacios, D., Stokes, C.R., Phillips, F.M., Clague, J.J., Alcalá-Reygosa, J., Andrés, N., Angel, I., Blard, P.-H., Briner, J.P., Hall, B.L., Dahms, D., Hein, A.S., Jomelli, V., Mark, B.G., Martini, M.A., Moreno, P., Riedel, J., Sagredo, E., Stansell, N.D., Vázquez-Selem, L., Vuille, M., Ward, D.J., 2020. The deglaciation of the Americas during the Last Glacial Termination. *Earth Sci. Rev.* 203, 103113. <https://doi.org/10.1016/j.earscirev.2020.103113>.
- Parker, A., 1970. An index of weathering for silicate rocks. *Geol. Mag.* 107 (6), 501–504.
- Pigati, J.S., Lifton, N.A., 2004. Geomagnetic effects on time-integrated cosmogenic nuclide production with emphasis on in situ ^{14}C and ^{10}Be . *Earth Planet. Sci. Lett.* 226 (1–2), 193–205.
- Portes, R., Dahms, D., Brandová, D., Raab, G., Christl, M., Kühn, P., Ketterer, M., Egli, M., 2018. Evolution of soil erosion rates in alpine soils of the Central Rocky Mountains using fallout Pu and $\delta^{13}\text{C}$. *Earth Planet. Sci. Lett.* 496, 258–269. <https://doi.org/10.1016/j.epsl.2018.06.002>.
- Quénard, L., Samouëlian, A., Laroche, B., Cornu, S., 2011. Lessivage as a major process of soil formation: A reevaluation of existing data. *Geoderma* 167–168, 135–147.
- Raab, G., Martin, A.P., Norton, K.P., Christl, M., Scarciglia, F., Egli, M., 2021. Complex patterns of schist tor exposure and surface uplift, Otago (New Zealand). *Geomorphology* 389, 107849.
- Raab, G., Scarciglia, F., Norton, K., Dahms, D., Brandová, D., Portes, R., Christl, M., Ketterer, M.E., Ruppli, A., Egli, M., 2018. Denudation Variability of the Sila Massif Upland (Italy) from decades to millennia using ^{10}Be and $^{239+240}\text{Pu}$. *Land Degrad. Dev.* 29, 3736–3752.
- Raab, G., Egli, M., Norton, K., Dahms, D., Brandová, D., Christl, M., Scarciglia, F., 2019. Climate and relief-induced controls on the temporal variability of denudation rates in a granitic upland. *Earth Surf. Proc. Land.* 44 (13), 2570–2586.
- Rea, B., Evans, D., 2005. Plateau icefield landsystems. In: Evans, D. (Ed.), *Glacial Landsystems*. Hodder Arnold, London, pp. 407–431.
- Reiter, W., Elfert, S., Glotzbach, C., Bernet, M., Spiegel, C., 2013. Relations between denudation, glaciation, and sediment deposition: implications from the Plio-Pleistocene Central Alps. *Basin Res.* 25 (6), 659–674.
- Ruxton, B.P., 1968. Measures of the degree of chemical weathering of rocks. *J. Geol.* 76 (5), 518–527.
- Schaller, M., Ehlers, T.A., Blum, J.D., 2010. Soil transport on a moraine foreslope. *Geomorphology* 115 (1–2), 117–128.
- Stone, J.O., 2000. Air pressure and cosmogenic isotope production. *J. Geophys. Res.* 105 (B10), 23753–23759.
- Takahashi, Y., Minai, Y., Ambe, S., Makide, Y., Ambe, F., 1999. Comparison of adsorption behavior of multiple inorganic ions on kaolinite and silica in the presence of humic acid using the multitracer technique. *Geochim. Cosmochim. Acta* 63 (6), 815–836.
- Van Den Brink, L.M., Janssen, C.R., 1985. The effect of human activities during cultural phases on the development of montane vegetation in the Serra da Estrela, Portugal. *Rev. Palaeobotany Palinol.* 44, 193–205.
- Van der Knaap, W.O., Van Leeuwen, J.F.N., 1995. Holocene vegetation succession and degradation as responses to climatic change and human activity in the Serra da Estrela, Portugal. *Rev. Palaeobotany Palynol.* 89, 153–211.
- Van der Knaap, W.O., Van Leeuwen, J.F.N., 1997. Holocene vegetation successions, altitudinal vegetation zonation, and climatic change in the Serra da Estrela. *Rev. Paleobot. Palynol.* 97, 239–285.
- von Blanckenburg, F., Belshaw, N.S., O’Nions, R.K., 1996. Separation of ^9Be and cosmogenic ^{10}Be from environmental materials and SIMS isotope dilution analysis. *Chem. Geol.* 129 (1–2), 93–99. [https://doi.org/10.1016/0009-2541\(95\)00157-3](https://doi.org/10.1016/0009-2541(95)00157-3).
- Vieira, G.T., Mora, C., Ramos, M., 2003. Ground temperature regimes and geomorphological implications in a Mediterranean mountain (Serra da Estrela, Portugal). *Geomorphology* 52 (1–2), 57–72.
- Vieira, G., 2004. Geomorfologia dos planaltos e altos vales da Serra da Estrela. *Ambientes frios do Plistocénico Superior e dinâmica actual*. PhD dissertation in Geography (Physical Geography), University of Lisbon, Portugal.
- Vieira, G., 2008. Combined numerical and geomorphological reconstruction of the Serra da Estrela plateau icefield, Portugal. *Geomorphology* 97 (1–2), 190–207.
- Vieira, G., Palacios, D., Mora, C., Andrés, N., Vázquez Selem, L., Castro E., 2017. Lagoa Seca: a key geosite in the Estrela Aspiring Geopark. In: International Conference Managing Mediterranean Geoheritage. Manteigas, 6–7 May 2017, AGE.
- Vieira, G., Nieuwendam, A., 2020. Glacial and Periglacial landscapes of the Serra da Estrela. In: Vieira G., Zézere, J.L., Mora, C. (Eds.), *Landforms and Landscapes of Portugal*, Springer: 185–198.
- Vieira, G., Palacios, D., Andrés, N., Mora, C., Vázquez Selem, L., Woronko, B., Soncco, C., Úbeda, J., Goyanes, G., 2021. Penultimate Glacial Cycle glacier extent in the Iberian Peninsula: New evidence from the Serra da Estrela (Central System, Portugal). *Geomorphology* 388, 107781. <https://doi.org/10.1016/j.geomorph.2021.107781>.
- Wainwright, J., Thornes, J.B., 2004. *Environmental Issues in the Mediterranean: Process and Perspectives from the Past to the Present*. Routledge, London, U.K.
- Wallbrink, P.J., Murray, A.S., 1993. Use of fallout radionuclides as indicators of erosion processes. *Hydrol. Process.* 7 (3), 297–304. <https://doi.org/10.1002/hyp.3360070307>.
- Walling, D.E., He, Q., 1999. Improved models for estimating soil erosion rates from cesium-137 measurements. *J. Environ. Qual.* 28 (2), 611–622. <https://doi.org/10.2134/jeq1999.00472425002800020027x>.
- Willenbring, J.K., von Blanckenburg, F., 2010. Long-term stability of global erosion rates and weathering during late-Cenozoic cooling. *Nature* 465 (7295), 211–214.
- Williams, H.B., Koppes, M.N., 2019. A comparison of glacial and paraglacial denudation responses to rapid glacial retreat. *Ann. Glaciol.* 60 (80), 151–164.
- Yu, F., Hunt, A., Egli, M., Raab, G., 2019. Comparison and contrast in soil depth evolution for steady state and stochastic erosion processes: Possible implications for landslide prediction. *Geochem. Geophys. Geosyst.* 20 (6), 2886–2906.
- Yu, F., Hunt, A.G., 2017. Damköhler Number Input to Transport-Limited Chemical Weathering Calculations. *ACS Earth Space Chem.* 1 (1), 30–38.
- Zhang, X., Higgitt, D.L., Walling, D.E., 1990. A preliminary assessment of the potential for using caesium-137 to estimate rates of soil erosion in the Loess Plateau of China. *Hydrol. Sci. J.* 35 (3), 243–252. <https://doi.org/10.1080/02626669009492427>.
- Zollinger, B., Alewell, C., Kneisel, C., Meusbürger, K., Brandová, D., Kubik, P., Egli, M., 2015. The effect of permafrost on time-split soil erosion using radionuclides (^{137}Cs , $^{239+240}\text{Pu}$, meteoric ^{10}Be) and stable isotopes ($\delta^{13}\text{C}$) in the eastern Swiss Alps. *J. Soils Sediments* 15 (6), 1400–1419. <https://doi.org/10.1007/s11368-014-0881-9>.